

Circumnuclear Media of Quiescent Supermassive Black Holes

Aleksey Generozov^{*}, Nicholas C. Stone, Brian D. Metzger

Columbia Astrophysics Laboratory, Columbia University, 550 West 120th Street, New York, NY 10027

5 October 2018

ABSTRACT

We calculate steady-state, one-dimensional hydrodynamic profiles of hot gas in slowly accreting (“quiescent”) galactic nuclei for a range of central black hole masses M_{\bullet} , parametrized gas heating rates, and observationally-motivated stellar density profiles. Mass is supplied to the circumnuclear medium by stellar winds, while energy is injected primarily by stellar winds, supernovae, and black hole feedback. Analytic estimates are derived for the stagnation radius (where the radial velocity of the gas passes through zero) and the large scale gas inflow rate, \dot{M} , as a function of M_{\bullet} and the gas heating efficiency, the latter being related to the star-formation history. We assess the conditions under which radiative instabilities develop in the hydrostatic region near the stagnation radius, both in the case of a single burst of star formation and for the average star formation history predicted by cosmological simulations. By combining a sample of measured nuclear X-ray luminosities, L_X , of nearby quiescent galactic nuclei with our results for $\dot{M}(M_{\bullet})$ we address whether the nuclei are consistent with accreting in a steady-state, thermally-stable manner for radiative efficiencies predicted for radiatively inefficient accretion flows. We find thermally-stable accretion cannot explain the short average growth times of low mass black holes in the local Universe, which must instead result from gas being fed in from large radii, due either to gas inflows or thermal instabilities acting on larger, galactic scales. Our results have implications for attempts to constrain the occupation fraction of SMBHs in low mass galaxies using the mean $L_X - \dot{M}_{\bullet}$ correlation, as well as the predicted diversity of the circumnuclear densities encountered by relativistic outflows from tidal disruption events.

Key words: black hole physics – galaxies: active

1 INTRODUCTION

Supermassive black holes (SMBHs) lurk in the centres of most, if not all nearby galaxies (see reviews by, e.g. [Kormendy & Richstone 1995](#); [Ferrarese & Ford 2005](#)). However, only a few percent of these manifest themselves as luminous active galactic nuclei (AGN). Nearly quiescent SMBHs, such as those hosting low luminosity AGN, constitute a silent majority (e.g. [Ho 2009](#)).

Understanding why most SMBHs appear to be inactive requires characterizing their gaseous environments. Gas near the SMBH sphere of influence, hereafter denoted the ‘circumnuclear medium’ (CNM), controls the mass accretion rate, \dot{M}_{\bullet} . The accretion rate in turn determines the SMBH luminosity and the feedback of its energy and momentum output on larger scales. Dense gas in the nucleus may lead to runaway cooling, resulting in bursty episodes of star formation and AGN activity (e.g. [Ciotti & Ostriker 2007](#)).

Knowledge of how \dot{M}_{\bullet} depends on the SMBH mass, M_{\bullet} , and other properties of the nucleus informs key questions related to the co-evolution of SMBHs and their host galaxies with cosmic time (e.g. [Kormendy & Ho 2013a](#); [Heckman & Best 2014](#)). In the low redshift Universe, SMBH growth is dominated by low mass black holes, $M_{\bullet} \lesssim 10^8 M_{\odot}$ (e.g. [Heckman et al. 2004](#)), a fact often attributed to the trend of ‘cosmic down-sizing’ resulting from hierarchical structure growth (e.g. [Gallo et al. 2008](#)). However, the physical processes by which typical low mass black holes accrete could in principle be distinct from those operating at higher SMBH masses, or those in AGN. Of key importance is whether SMBHs grow primarily by the accretion of gas fed in directly from galactic or extragalactic scales, or whether significant growth can result also from local stellar mass loss in the nuclear region.

A better understanding of what mechanisms regulate accretion onto quiescent SMBHs would shed new light on a variety of observations, such as the occupation fraction of SMBHs in low mass galaxies. [Miller et al. \(2015\)](#) use the av-

^{*} E-mail: ag@astro.columbia.edu

erage relationship between the nuclear X-ray luminosities, L_X , of a sample of early type galaxies and their associated SMBH masses to tentatively infer that the SMBH occupation fraction becomes less than unity for galaxies with stellar masses $M_\star \lesssim 10^{10} M_\odot$ ($M_\bullet \lesssim 10^7 M_\odot$). This method relies on extrapolating a power-law fit of the $L_X - M_\bullet$ distribution to low values of L_X below the instrument detection threshold, an assumption which is questionable if different physical processes control the accretion rates onto the lowest mass SMBHs.

The gas density in galactic nuclei also influences the emission from stellar tidal disruption events (TDEs), such as the high energy transient *Swift* J1644+57 (Bloom et al. 2011, Burrows et al. 2011; Levan et al. 2011; Zauderer et al. 2011). This event was powered by an impulsive relativistic jet, which produced synchrotron radio emission as the jet material decelerated from shock interaction with the CNM of the previously quiescent SMBH (Giannios & Metzger 2011; Zauderer et al. 2011). Modeling of J1644+57 showed that the CNM density was much lower than that measured surrounding Sgr A* on a similar radial scale (Berger et al. 2012; Metzger et al. 2012). However, a TDE jet which encounters a denser CNM would be decelerated more rapidly, producing different radio emission than in J1644+57. Variations in the properties of the CNM could help explain why most TDEs appear to be radio quiet (e.g. Bower et al. 2013; van Velzen et al. 2013).

Gas comprising the CNM of quiescent (non-AGN) galaxies can in principle originate from several sources: (1) wind mass loss from predominantly evolved stars; (2) stellar binary collisions; and (3) unbound debris from a recent TDE. Stellar wind mass loss is probably the dominant source insofar as collisions are relevant only in extremely dense stellar environments for very young stellar populations (Rubin & Loeb 2011), while MacLeod et al. (2013) find that TDEs contribute subdominantly to the time-averaged accretion rate of quiescent SMBHs.

The gas inflow rate on large scales is much easier to constrain both observationally and theoretically than the black hole (horizon scale) accretion rate. Ho (2009) determines the inflow rates in a sample of early-type galaxies by using X-ray observations to determine the Bondi accretion rate, and also by using estimated mass loss rates of evolved stars. Both methods lead him to conclude that the available gas reservoir is more than sufficient to power the observed low-luminosity AGN, assuming the standard ~ 10 per cent radiative efficiency for thin disc accretion. Several lines of evidence now suggest that low-luminosity AGN result from accretion proceeding in a radiatively inefficient mode (Yuan & Narayan 2014), due either to the advection of gravitationally-released energy across the SMBH horizon (e.g. Narayan & Yi 1995) or due to disc outflows, which reduce the efficiency with which the inflowing gas ultimately reaches the SMBH (e.g. Blandford & Begelman 1999; Li et al. 2013).

Another approach to determine the inflow rates, which we adopt in this paper, is to directly calculate the density, velocity and temperature profiles of the CNM using a physically motivated hydrodynamic model. Mass is injected into the nuclear environment via stellar winds, while energy is input from several sources including stellar winds, supernovae (SNe), and AGN feedback (Quataert 2004; De Colle et al. 2012; Shcherbakov et al. 2014). Unlike previous works, which

focused primarily on modeling individual galaxies, here we model the CNM properties across a representative range of galaxy properties, including different SMBH masses, stellar density profiles, and star formation histories (SFHs).

Previous studies, employing multi-dimensional numerical hydrodynamics and including variety of (parametrized) physical effects, have focused on massive elliptical galaxies (e.g. Ciotti & Ostriker 2007; Ciotti et al. 2010). These works show the periodic development of cooling instabilities on galactic scales, which temporarily increase the gas inflow rate towards the nucleus until feedback becomes strong enough to shut off the flow and halt SMBH growth.

In this paper we focus on time-independent models, in which the nuclear gas receives sufficient heating to render radiative cooling negligible. This approach allows us to systematically explore the relevant parameter space and to derive analytic expressions that prove useful in determining under what conditions cooling instabilities manifest in the nuclear region across the expected range of galaxy properties, or whether other (non-AGN) forms of feedback can produce a prolonged state of steady, thermally stable accretion. Even if cooling instabilities develop on galactic scales over longer \sim Gyr time-scales, we aim to explore whether a quasi steady-state may exist between these inflow events on smaller radial scales comparable to the sphere of influence.

In the presence of strong heating, one-dimensional steady-state flow is characterized by an inflow-outflow structure, with a critical radius known as the “stagnation radius” r_s where the radial velocity passes through zero. Mass loss from stars interior to the stagnation radius is accreted, while that outside r_s is unbound in an outflow from the nucleus. The stagnation radius, rather than the Bondi radius, thus controls the inflow rate (although we will show that r_s usually resides near the nominal Bondi radius). When heating is sufficiently weak, however, the stagnation radius may move to much larger radii or not exist at all, significantly increasing the inflow rate the SMBH, i.e. a “cooling flow”. However, the hydrostatic nature of gas near the stagnation radius also renders the CNM at this location particularly susceptible to local thermal instabilities, the outcome of which could well be distinct from the development of a cooling flow.

This paper is organized as follows. In §2 we describe our model, including the sample of galaxy properties used in our analysis (§2.1) and our numerical procedure for calculating the steady-state hydrodynamic profile of the CNM (§2.2). In §3 we describe our analytic results, which are justified via the numerical solutions we present in §4. We move from a general and parametrized treatment of heating to a physically motivated one in §5, where we consider a range of physical processes that can inject energy into the CNM. In §6 we discuss the implications of our results for topics which include the nuclear X-ray luminosities of quiescent black holes, jetted TDEs, and the growth of SMBHs in the local Universe. In §7 we summarize our conclusions. Table 1 provides the definitions of commonly used variables. Appendix A provides useful analytic results for the stagnation radius, while Appendix B provides the details of our method for calculating stellar wind heating and mass input.

Table 1. Definitions of commonly used variables

Variable	Definition
M_\bullet	Black hole mass
\tilde{v}_w	Total heating parameter, including minimum heating rate from stellar and black hole velocity dispersion
v_w	Total heating parameter, excluding minimum heating rate from velocity dispersion
σ_0	Stellar velocity dispersion (assumed to be radially constant).
t_{dyn}	r/σ_0 : Dynamical time at large radii (where stellar potential dominates)
t_{ff}	$(r^3/(GM_\bullet))^{1/2}$: Free fall time (where the black hole potential dominates)
ζ	Alternative heating parameter, $\zeta \equiv \sqrt{1 + (v_w/\sigma_0)^2}$ (eq. [16])
r_s	Stagnation radius, where gas radial velocity goes to zero
r_{inf}	Radius of sphere of influence (eq. [3])
r_b	Outer break radius of stellar density profile
r_{Ia}	Radius interior to which SN Ia are infrequent compared to the dynamical time-scale (eq. [36])
$\rho_\star(r)$	3D radial stellar density profile
$\rho(r)$	Gas density of CNM
$M_\star(r)$	Total enclosed stellar mass inside radius r
$M_{\text{enc}}(r)$	Total enclosed mass inside radius r (SMBH + stars)
$q(r)$	Mass source term due to stellar winds, $q \propto \rho_\star$ (eq. [8])
η	Parameter setting normalization of mass input from stellar winds (eq. [8])
τ_\star	Age of stellar population, in case of a single burst of star formation
Γ	Power-law slope of radial stellar surface brightness profile interior to the break radius
δ	Power-law slope of the 3D stellar density profile inside of the break radius, $\delta \equiv \Gamma + 1$.
\dot{M}	Large scale inflow rate (not necessarily equal to the SMBH accretion rate)
\dot{M}_\bullet	SMBH accretion rate, $\dot{M}_\bullet = \alpha \dot{M}$, where $\alpha < 1$ accounts for outflows from the accretion disc on small scales.
\dot{M}_{Ia}	Maximum accretion rate as limited by SN Ia (eq. [39])
\dot{M}_C	Equilibrium inflow rate set by Compton heating acting alone (eq. [46])
\dot{M}_{TI}	Maximum accretion rate for thermally stable accretion (eq. [29])
$\dot{q}_{\text{heat}}/\dot{q}_{\text{rad}}$	Ratio of external heating (stellar winds, SN Ia, MSPs) to radiative cooling (eq. [25])
t_h	Hubble time-scale
ν	Gas density power-law slope at the stagnation radius (eq. [13])

2 MODEL

2.1 Galaxy models

Lauer et al. (2007) use *Hubble Space Telescope* WFPC2 imaging to measure the radial surface brightness profiles for hundreds of nearby early type galaxies. The measured profile is well fit by a ‘‘Nuker’’ law parameterization:

$$I(\xi) = I_b 2^{(\beta-\Gamma)/\alpha} \xi^{-\Gamma} (1 + \xi^\alpha)^{-(\beta-\Gamma)/\alpha}, \quad \xi \equiv \frac{r}{r_b}, \quad (1)$$

i.e., a broken power law that transitions from an inner power law slope, Γ , to an outer power law slope, β , at a break radius, r_b . If the stellar population is spherically symmetric, then this corresponds to a 3D stellar density $\rho_\star \propto r^{-1-\Gamma}$ for $r \ll r_b$ and $\rho_\star \propto r^{-1-\beta}$ for $r \gg r_b$. We can write the deprojected stellar density approximately (formally, this is the $\alpha \rightarrow \infty$ limit) as

$$\rho_\star = \begin{cases} \rho_\star|_{r_{\text{inf}}} (r/r_{\text{inf}})^{-1-\Gamma} & r \leq r_b \\ \rho_\star|_{r_b} (r/r_b)^{-1-\beta} & r > r_b, \end{cases} \quad (2)$$

where $\rho_\star|_{r_{\text{inf}}}$ is the stellar density at the radius of the black hole sphere of influence¹,

$$r_{\text{inf}} \simeq GM_\bullet/\sigma_\bullet^2 \approx 14M_\bullet^{0.6} \text{ pc}, \quad (3)$$

¹ This approximate expression agrees surprisingly well with the mean empirical scaling relation for $r_{\text{inf}}(M_\bullet)$ calculated in appendix C of Stone & Metzger (2014), although we note that this relation has significant scatter. Also, we note that the scaling is somewhat different for cores and cusps. Fixing the power law

where $M_{\bullet,s} \equiv M_\bullet/10^8 M_\odot$ and the second equality in (3) employs the $M_\bullet - \sigma$ relationship of McConnell et al. (2011),

$$M_\bullet \simeq 2 \times 10^8 \left(\frac{\sigma_\bullet}{200 \text{ km s}^{-1}} \right)^{5.1} M_\odot. \quad (4)$$

This may be of questionable validity for low mass black holes (e.g., Greene et al. 2010; Kormendy & Ho 2013b). Also, several of the black hole masses used in McConnell et al. (2011) were underestimated (Kormendy & Ho 2013b). However, our results are not overly sensitive to the exact form of the $M_\bullet - \sigma$ relationship that we use.

A galaxy model is fully specified by four parameters: M_\bullet , Γ , r_b , and β . We compute models for three different black hole masses, $M_\bullet = 10^6, 10^7, 10^8 M_\odot$. The distribution of Γ in the Lauer et al. (2007) sample is bimodal, with a concentration of ‘‘core’’ galaxies with $\Gamma < 0.3$ and a concentration of ‘‘cusp’’ galaxies with $\Gamma > 0.5$. We bracket these possibilities by considering models with $\Gamma = 0.8$ and $\Gamma = 0.1$.

We fix $\beta = 2$ but find that our results are not overly sensitive to the properties of the gas flow on radial scales $\gtrsim r_b$. The presence of the break radius r_b is, however, necessary to obtain a converged steady state for some regions of our parameter space². We consider solutions calculated for up to four values of r_b : 50 pc, 100 pc, 200 pc, and 400 pc,

slope, $r_{\text{inf}} \simeq 25(8)M_\bullet^{0.6}$ for core (cusp) galaxies. We will use separate scaling relations for r_{inf} for cores and cusps unless otherwise noted.

² In addition, for $\beta \leq 2$ the stellar density must steepen at still

motivated by the range of break radii from the [Lauer et al. \(2007\)](#) sample.³ We neglect values of r_b which would give unphysically large bulges for a given M_\bullet .

Finally, we note that [Lauer et al. 2005](#) find that $\sim 60\%$ of cusp galaxies and $\sim 29\%$ of core galaxies have (generally unresolved) emission in excess of the inward extrapolation of the Nuker law. Indeed, some low mass galaxies with $M_\bullet \lesssim 10^8 M_\odot$ possess nuclear star clusters ([Graham & Spitler 2009](#)), which are not accounted for by our simple parametrization of the stellar density. In such cases gas and energy injection could be dominated by the cluster itself, i.e. concentrated within its own pc-scale ‘‘break radius’’ which is much smaller than the outer break in the older stellar population on much larger scales. Although our analysis does not account for such an inner break, we note that for high heating rates the stagnation radius and concomitant inflow rate are not sensitive to the break radius.

2.2 Hydrodynamic Equations

Following [Quataert \(2004, see also Holzer & Axford 1970; De Colle et al. 2012; Shcherbakov et al. 2014\)](#), we calculate the density ρ , temperature T , and radial velocity v of the CNM for each galaxy model by solving the equations of one-dimensional, time-dependent hydrodynamics,

$$\frac{\partial \rho}{\partial t} + \frac{1}{r^2} \frac{\partial}{\partial r} (\rho r^2 v) = q \quad (5)$$

$$\rho \left(\frac{\partial v}{\partial t} + v \frac{\partial v}{\partial r} \right) = - \frac{\partial p}{\partial r} - \rho \frac{GM_{\text{enc}}}{r^2} - qv \quad (6)$$

$$\rho T \left(\frac{\partial s}{\partial t} + v \frac{\partial s}{\partial r} \right) = q \left[\frac{v^2}{2} + \frac{\tilde{v}_w^2}{2} - \frac{\gamma}{\gamma - 1} \frac{p}{\rho} \right], \quad (7)$$

where p and s are the pressure and specific entropy, respectively, and $M_{\text{enc}} = M_\star(r) + M_\bullet$ is the enclosed mass (we neglect dark matter contributions). We adopt an ideal gas equation of state with $p = \rho kT / \mu m_p$ with $\mu = 0.62$ and $\gamma = 5/3$. The source term in equation (5),

$$q = \frac{\eta \rho_\star}{t_h}, \quad (8)$$

represents mass input from stellar winds, which we parametrize in terms of the fraction η of the stellar density ρ_\star being recycled into gas on the Hubble time $t_h = 1.4 \times 10^{10}$ yr. To good approximation $\eta \simeq 0.02 (\tau_\star / t_h)^{-1.3}$ at time τ_\star following an impulsive starburst (e.g., [Ciotti et al. 1991](#))⁴, although η is significantly higher for continuous SFHs (bottom panel of Fig. 7).

Source terms $\propto q$ also appear in the momentum and entropy equations (eqs. [6] and [7]) because the isotropic injection of mass represents, in the SMBH rest frame, a source

larger radii to avoid the mass enclosed diverging to infinity. However, we do not find it necessary to include this outer break.

³ For the core galaxies the break radius follows the scaling relationship $r_b \sim 90 (M_\bullet, 8)^{0.5}$ pc, with scatter of approximately one dex. Most of the cusp galaxies have r_b between 100 and 1000 pc, and lack a clear trend with M_\bullet . The mean r_b for cusp galaxies in the [Lauer et al. \(2007\)](#) sample is ~ 240 pc.

⁴ [Ciotti et al. \(1991\)](#) give the mass return rate from evolved stars as a function of B-band luminosity instead of volumetrically, but our expressions are equivalent.

of momentum and energy relative to the mean flow. Physically, these result from the mismatch between the properties of virialized gas injected by stellar winds and the mean background flow. The term $\propto p/\rho = c_s^2$ is important because it acts to stabilize the flow against runaway cooling (§3.4).

The term $\propto \tilde{v}_w^2 = \sigma(r)^2 + v_w^2$ in the entropy equation accounts for external heating sources (e.g., [Shcherbakov et al. 2014](#)), where

$$\sigma \approx \sqrt{\frac{3GM_\bullet}{(\Gamma + 2)r}} + \sigma_0^2, \quad (9)$$

is the stellar velocity dispersion. This accounts for the minimal amount of shock heating from stellar winds due to the random motion of stars in the SMBH potential. We take σ_0 to be constant and use $\sigma_0^2 \approx 3\sigma_\bullet^2$, where $\sigma_\bullet \simeq 170 M_\bullet^{0.2}$ km/s is the velocity dispersion from the [McConnell et al. \(2011\)](#) $M_\bullet - \sigma$ relation. The second term, v_w^2 , parametrizes additional sources of energy input, including faster winds from young stars, millisecond pulsars (MSPs), supernovae, AGN feedback, etc (§5). We assume that v_w is constant with radius, i.e. that the volumetric heating rate is proportional to the local stellar density.

Our model does not take into account complications such as more complicated geometries or the discrete nature of real stars ([Cuadra et al. 2006, 2008](#)). In the case of Sgr A* these effects reduce the time-averaged inflow rate to $\sim 10^{-6} M_\odot \text{yr}^{-1}$ – an order of magnitude less than a 1D spherical model ([Cuadra et al. 2006](#)). Motions of individual stars can produce order of magnitude spikes in the accretion rate ([Cuadra et al. 2008](#)).

To isolate the physics of interest, our baseline calculations neglects three potentially important effects: heat conduction, radiative cooling, and rotation. Heat conduction results in an additional heating term in equation (7),

$$\dot{q}_{\text{cond}} = \nabla \cdot (\kappa \nabla T), \quad (10)$$

where $\kappa = \kappa_{\text{spitz}} / (1 + \psi)$ ([Dalton & Balbus 1993](#)) is the conductivity and $\kappa_{\text{spitz}} = \kappa_0 T^{5/2}$ is the classical [Spitzer \(1962\)](#) value ($\kappa_0 \simeq 2 \times 10^{-6}$ in cgs units). The flux limiter $\psi = \kappa_{\text{spitz}} \nabla T / (5\phi \rho c_s^3)$ saturates the conductive flux if the mean free path for electron coulomb scattering exceeds the temperature length scale, where $c_s \equiv (kT / \mu m_p)^{1/2}$ is the isothermal sound speed and $\phi \lesssim 1$ is an uncertain dimensionless constant (we adopt $\phi = 0.1$). Even a weak magnetic field that is oriented perpendicular to the flow could suppress the conductivity by reducing the electron mean free path. However, for radially-decreasing temperature profiles of interest, the flow is susceptible to the magneto-thermal instability ([Balbus 2001](#)), the non-linear evolution of which results in a radially-directed field geometry ([Parrish & Stone 2007](#)). In §3.3 we show that neglecting conductivity results in at most order-unity errors in the key properties of the solutions.

Radiative cooling contributes an additional term to equation (7), of the form

$$\dot{q}_{\text{rad}} = -\Lambda(T)n^2, \quad (11)$$

where $n \equiv \rho / \mu m_p$ and $\Lambda(T)$ is the cooling function. We neglect radiative cooling in our baseline calculations, despite the fact that this is not justified when the wind heating

v_w is low or if the mass return rate η is high. Once radiative cooling becomes comparable to other sources of heating and cooling, its presence can lead to thermal instability (e.g. Gaspari et al. 2012b, McCourt et al. 2012, Li & Bryan 2014a) that cannot be accounted for by our 1D time-independent model. Our goal is to use solutions which neglect radiation to determine over what range of conditions cooling instabilities will develop (§3.4).

Equations (5)-(7) are solved using a sixth order finite difference scheme with a third order Runge-Kutta scheme for time integration and artificial viscosity terms in the velocity and entropy equations for numerical stability (Brandenburg 2003)⁵. We assume different choices of $v_w = 300, 600, 1200$ km s⁻¹ spanning a physically plausible range of thermally stable heating rates. Although we are interested in the steady-state inflow/outflow solution (assuming one exists), we solve the time-dependent equations to avoid numerical issues that arise near the critical sonic points.

Our solutions can be scaled to any value of the mass input parameter, η , since the mass and energy source terms scale linearly with ρ or ρ_* ; however, the precise value of η must be specified when cooling or thermal conduction are included. We check the accuracy of our numerical solutions by confirming that mass is conserved across the grid, in addition to the integral constraint on the energy (Bernoulli integral).

3 ANALYTIC RESULTS

We first describe analytic estimates of physical quantities, such as the stagnation radius r_s and the mass inflow rate, the detailed derivation of which are given in Appendix A.

3.1 Flow Properties Near the Stagnation Radius

Continuity of the entropy derivative at the stagnation radius where $v = 0$ requires that the temperature at this location be given by (eq. [A2])

$$T|_{r_s} = \frac{\gamma - 1}{\gamma} \frac{\mu m_p \tilde{v}_w^2}{2k} \underset{v_w \gg \sigma_0}{\approx} \frac{\gamma - 1}{\gamma} \frac{\mu m_p v_w^2}{2k} \frac{13 + 8\Gamma}{13 + 8\Gamma - 6\nu} \approx \begin{cases} 5.0 \times 10^6 v_{500}^2 \text{ K} & \text{core} \\ 5.5 \times 10^6 v_{500}^2 \text{ K} & \text{cusp,} \end{cases} \quad (12)$$

where $v_{500} \equiv v_w / (500 \text{ km s}^{-1})$ and $\nu \equiv -d \ln \rho / d \ln r|_{r_s}$ is the density power-law slope at $r = r_s$. Empirically, we find from our numerical solutions that

$$\nu \simeq \frac{1}{6} (4\Gamma + 3) \quad (13)$$

Hydrostatic equilibrium likewise determines the value of the stagnation radius (Appendix A, eq. A6)

$$r_s = \frac{GM_\bullet}{\nu \tilde{v}_w^2} \left[\frac{13 + 8\Gamma}{4 + 2\Gamma} \right] = \frac{GM_\bullet}{\nu(v_w^2 + \sigma_0^2)} \left[4 \frac{M_\star|_{r_s}}{M_\bullet} + \frac{13 + 8\Gamma}{4 + 2\Gamma} - \frac{3\nu}{2 + \Gamma} \right] \quad (14)$$

⁵ code is available at <https://github.com/alekseygenozov/hydro>

For high heating rates $v_w \gg \sigma_0$, the stagnation radius resides well inside the SMBH sphere of influence. In this case $M_\star|_{r_s}/M_\bullet \ll 1$, such that equation (14) simplifies to

$$r_s \underset{v_w \gg \sigma_0}{\approx} \left(\frac{13 + 8\Gamma}{4 + 2\Gamma} - \frac{3\nu}{2 + \Gamma} \right) \frac{GM_\bullet}{\nu v_w^2} \approx \begin{cases} 8 \text{ pc } M_{\bullet,8} v_{500}^{-2} \text{ yr}^{-1} & \text{core} \\ 4 \text{ pc } M_{\bullet,8} v_{500}^{-2} \text{ yr}^{-1} & \text{cusp,} \end{cases} \quad (15)$$

where we have used equation (13) to estimate ν separately for core ($\Gamma = 0.1$; $\nu \approx 1$) and cusp ($\Gamma = 0.8$; $\nu \approx 0.6$) galaxies. This expression is similar to that obtained by Volonteri et al. (2011) on more heuristic grounds (their eq. 6).

In the opposite limit of weak heating ($v_w \lesssim \sigma_0$) the stagnation radius moves to large radii, approaching the break radius r_b in the stellar density profile, implying that all of the interstellar medium (ISM) inside of r_b is inflowing. In particular, we find that r_s approaches r_b for heating below a critical threshold

$$\zeta \equiv \sqrt{1 + \left(\frac{v_w}{\sigma_0} \right)^2} < \zeta_c \approx \sqrt{\left(\frac{r_b}{r_{\text{inf}}} \right)^{(1-\Gamma)} + 1} \quad (16)$$

Condition (16) approximately corresponds to the requirement that the heating rate exceed the local escape speed at the break radius, r_b . This result makes intuitive sense: gas is supplied to the nucleus by stars which are gravitationally bound to the black hole, so outflows are possible only if the specific heating rate $\sim v_w^2$ significantly exceeds the specific gravitational binding energy.

3.2 Inflow Rate

The large scale inflow rate towards the SMBH is given by the total mass loss rate interior to the stagnation radius (eq. [8]),

$$\dot{M} = 4\pi \int_0^{r_s} q r^2 dr = \frac{\eta M_\star|_{r_s}}{t_h} = \frac{\eta M_\bullet (r_s/r_{\text{inf}})^{2-\Gamma}}{t_h} \approx \begin{cases} 4.5 \times 10^{-5} M_{\bullet,8}^{1.76} v_{500}^{-3.8} \eta_{0.02} \text{ M}_\odot \text{ yr}^{-1} & \text{core} \\ 3.2 \times 10^{-5} M_{\bullet,8}^{1.48} v_{500}^{-2.4} \eta_{0.02} \text{ M}_\odot \text{ yr}^{-1} & \text{cusp,} \end{cases} \quad (17)$$

where we have assumed $v_w \gg \sigma_0$ by adopting equation (15) for r_s . The resulting Eddington ratio is given by

$$\frac{\dot{M}}{\dot{M}_{\text{edd}}} \approx \begin{cases} 2.0 \times 10^{-5} M_{\bullet,8}^{0.76} v_{500}^{-3.8} \eta_{0.02} & \text{core,} \\ 1.4 \times 10^{-5} M_{\bullet,8}^{0.48} v_{500}^{-2.4} \eta_{0.02} & \text{cusp,} \end{cases} \quad (18)$$

where $\dot{M}_{\text{edd}} = 2.2 M_{\bullet,8} M_\odot \text{ yr}^{-1}$ is the Eddington accretion rate, assuming a radiative efficiency of ten per cent. Note the sensitive dependence of the inflow rate on the wind heating rate. Equation (18) is the radial mass inflow rate on relatively large scales and does not account for outflows from the SMBH accretion disc (e.g. Blandford & Begelman 1999; Li et al. 2013), which may significantly reduce the fraction of \dot{M} that actually reaches the SMBH. Thus we distinguish between the large scale inflow rate, \dot{M} , and the accretion rate onto the black hole, \dot{M}_\bullet .

The gas density at the stagnation radius, $\rho|_{r_s}$, is more challenging to estimate accurately. By using an alternative estimate of \dot{M} as the gaseous mass within the stagnation

radius divided by the free-fall time $t_{\text{ff}}|_{r_s} = (r_s^3/GM_\bullet)^{1/2}$,

$$\dot{M} \sim \frac{(4\pi/3)r_s^3\rho|_{r_s}}{t_{\text{ff}}|_{r_s}}, \quad (19)$$

in conjunction with eqs. (17) and (15), we find that

$$\rho|_{r_s} \approx \begin{cases} 5.2 \times 10^{-26} M_{\bullet,8}^{-0.2} v_{500}^{-0.8} \eta_{0.02} \text{ g cm}^{-3} & \text{core,} \\ 1.0 \times 10^{-25} M_{\bullet,8}^{-0.5} v_{500}^{0.6} \eta_{0.02} \text{ g cm}^{-3} & \text{cusp} \end{cases} \quad (20)$$

It is useful to compare our expression for \dot{M} (eq. [17]) to the standard Bondi rate for accretion onto a point source from an external medium of specified density and temperature (Bondi 1952):

$$\dot{M}_B = 4\pi\lambda r_B^2 \rho|_{r_B} v_{\text{ff}}|_{r_B}, \quad (21)$$

where $r_B \equiv GM/c_{s,\text{ad}}^2$ is the Bondi radius, $c_{s,\text{ad}} = \sqrt{\gamma kT/\mu m_p}$ is the adiabatic sound speed, $v_{\text{ff}}|_{r_B} = r_B/t_{\text{ff}}|_{r_B} = (GM_\bullet/r_B)^{1/2}$ and λ is a parameter of order unity.

Equation (19) closely resembles the Bondi formula (eq. [21]) provided that r_B is replaced by r_s . Indeed, for $r_s < r_{\text{inf}}$ we have that (eq. [14])

$$r_s \approx \frac{13 + 8\Gamma}{4 + 2\Gamma} \frac{GM_\bullet}{v\tilde{v}_w^2} \approx \frac{13 + 8\Gamma}{(2 + \Gamma)(3 + 4\Gamma)} r_B, \quad (22)$$

where the second equality makes use of equation (12).

3.3 Heat Conduction

Our analytic derivations neglect the effects of heat conduction, an assumption we now check. The ratio of the magnitude of the conductive heating rate (eq. [10]) to the external heating rate at the stagnation radius is given by

$$\begin{aligned} \frac{\nabla \cdot (\kappa \nabla T)}{q\tilde{v}_w^2/2} \Big|_{r_s} &\sim \frac{2t_h \kappa_0 T|_{r_s}^{7/2}}{r_s^2 \eta \rho_\star |_{r_s} \tilde{v}_w^2} \left(1 + \frac{\kappa_0 T^{7/2}|_{r_s}}{5r_s \phi \rho c_s^3} \right)^{-1} \\ &\sim \min \begin{cases} 20\eta_{0.02}^{-1} M_{\bullet,8}^{-0.8} v_{500}^{6.8} & \text{unsaturated (core)} \\ 30\eta_{0.02}^{-1} M_{\bullet,8}^{-0.5} v_{500}^{5.4} & \text{unsaturated (cusp)} \\ 2\phi & \text{saturated,} \end{cases} \end{aligned} \quad (23)$$

where the second equality makes use of equations (12), (15), and we have made the approximations $\nabla^2 \sim 1/r_s^2$, $\nabla \sim 1/r_s$. The stellar density profile is approximated as (eq. [2])

$$\begin{aligned} \rho_\star|_{r_s} &\simeq \frac{M_\bullet(2 - \Gamma)}{4\pi r_{\text{inf}}^3} \left(\frac{r_s}{r_{\text{inf}}} \right)^{-1-\Gamma} \\ &\simeq \begin{cases} 7.9 \times 10^{-19} M_{\bullet,8}^{-1.2} v_{500}^{2.2} \text{ g cm}^{-3} & \text{core} \\ 2.3 \times 10^{-18} M_{\bullet,8}^{-1.5} v_{500}^{3.6} \text{ g cm}^{-3} & \text{cusp,} \end{cases} \end{aligned} \quad (24)$$

where the stagnation radius is assumed to reside well inside the Nuker break radius.

Equation (23) shows that, even when conduction is saturated, our neglecting of heat conduction near the stagnation radius results in at most an order unity correction for causal values of the saturation parameter $\phi < 0.1$. Our numerical experiments which include conductive heating confirm this (§4). We do not consider the possibility that the conduction of heat from the inner accretion flow can affect the flow on much larger scales (Johnson & Quataert 2007).

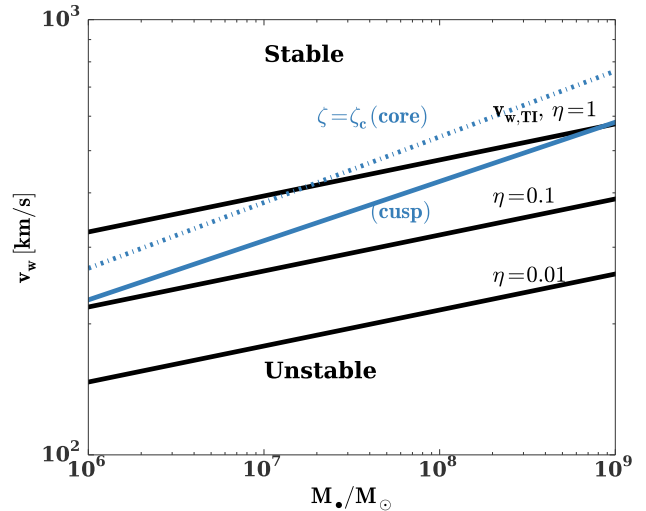


Figure 1. Minimum effective wind heating parameter required for thermal stability as a function of SMBH mass. Black lines show v_{TI} (eq. [27]), the heating rate required for $(\dot{q}_{\text{heat}}/\dot{q}_{\text{rad}})_{r_s} > 10$ in the high-heating limit when the stagnation radius lies interior to the influence radius, for different values of the mass loss parameter η as marked. Blue lines show the minimum heating parameter required to have $\zeta > \zeta_c = (r_b/r_{\text{inf}})^{0.5(1-\Gamma)}$ (eq. [16]), separately for cusp (solid) and core (dashed) galaxies. Based on the Lauer et al. (2007) sample we take $r_{\text{inf}} = 25(8)M_{\bullet,8}^{0.6} \text{ pc}$ and $r_b = 90M_{\bullet,8}^{0.5} \text{ pc}$ (240 pc) for cores (cusps). For $\zeta < \zeta_c$ the stagnation radius moves from inside the influence radius, out to the stellar break radius r_b . This renders the flow susceptible to thermal runaway, even if $v_w > v_{\text{TI}}$.

3.4 Thermal Instability

Radiative cooling usually has its greatest impact near or external to the stagnation radius, where the gas resides in near hydrostatic balance. If radiative cooling becomes important, it can qualitatively alter key features of the accretion flow. Initially hydrostatic gas is thermally unstable if the cooling time is much less than the free-fall time, potentially resulting in the formation of a multi-phase medium (Gaspari et al. 2012b, 2013, 2015; Li & Bryan 2014b).

Even if the hot plasma of the CNM does not condense into cold clouds, the loss of pressure can temporarily increase the inflow and accretion rates by producing a large-scale cooling flow. When coupled to feed-back processes which result from such enhanced accretion, this can lead to time-dependent limit cycle behavior (e.g. Ciotti & Ostriker 2007; Ciotti et al. 2010; Yuan & Li 2011, Gan et al. 2014), which is also inconsistent with our assumption of a steady, single-phase flow.

Cooling instability can, however, be prevented if destabilizing radiative cooling ($\dot{q}_{\text{rad}} \propto T^{-2.7}$) is overwhelmed by other sources of cooling, namely the *stabilizing* term $\propto -qc_s^2 \propto -T$ in the entropy equation (eq. [7]). Neglecting radiative cooling to first order, this term is balanced at the stagnation radius by the external heating term, $\dot{q}_{\text{heat}} = q\tilde{v}_w^2/2$. One can therefore assess thermal stability by comparing the ratio of external heating to radiative cool-

ing $|\dot{q}_{\text{rad}}|$ (eq. [11]),

$$\frac{\dot{q}_{\text{heat}}}{|\dot{q}_{\text{rad}}|}\bigg|_{r_s} \simeq \begin{cases} 630\eta_{0.02}^{-1}M_{\bullet,8}^{-0.76}v_{500}^{7.2} & , \text{core} \\ 660\eta_{0.02}^{-1}M_{\bullet,8}^{-0.48}v_{500}^{5.8} & , \text{cusp}, \end{cases} \quad (25)$$

where we have used equations (20) and (24) for the gas and stellar densities at the stagnation radius, respectively. We have approximated the cooling function for $T < 2 \times 10^7$ K as $\Lambda(T) = 1.1 \times 10^{-22} (T/10^6 \text{K})^{-0.7} \text{erg cm}^3 \text{s}^{-1}$, which assumes solar metallicity gas (Draine 2011; his Fig. 34.1).

To within a constant of order unity, equation (25) also equals the ratio of the gas cooling time-scale $t_{\text{cool}} \equiv (3nkT/2\mu)/|\dot{q}_{\text{rad}}|$ to the free-fall time t_{ff} at the stagnation radius. This equivalence can be derived using the equality

$$\rho|_{r_s} = \frac{3qt_{\text{ff}}|_{r_s}}{2 - \Gamma}. \quad (26)$$

that results by combining equations (17),(19), and (24). Sharma et al. (2012) argue cooling instability develops in a initially hydrostatic atmosphere if $t_{\text{cool}} \lesssim 10t_{\text{ff}}$, so equation (25) represents a good proxy for instability in this case as well.

Based on our numerical results (§4) and the work of Sharma et al. (2012) we define thermally stable flows according to the criterion $\dot{q}_{\text{heat}} > 10|\dot{q}_{\text{rad}}|$ ($t_{\text{cool}} > 10t_{\text{ff}}$) being satisfied near the stagnation radius. This condition translates into a critical minimum heating rate

$$v_w > v_{\text{TI}} \simeq \begin{cases} 280\eta_{0.02}^{0.14}M_{\bullet,8}^{0.11} \text{ km s}^{-1} & , \text{core} \\ 240\eta_{0.02}^{0.17}M_{\bullet,8}^{0.08} \text{ km s}^{-1} & , \text{cusp} \end{cases} \quad (27)$$

Equations (25) and (27) are derived using expressions for the stagnation radius and gas density in the high heating limit of $\zeta > \zeta_c = (r_b/r_{\text{inf}})^{0.5(1-\Gamma)}$ (eq. [16]). However, for $\zeta < \zeta_c$, the stagnation radius diverges to the break radius r_b . The quasi-hydrostatic structure that results in this case greatly increases the gas density, which in practice renders the flow susceptible to thermal runaway, even if $v_w > v_{\text{TI}}$ according to equation (27). In other words, the true condition for thermal instability can be written

$$v_w^2 > \max[v_{\text{TI}}^2, \sigma_0(r_b/r_{\text{inf}})^{(1-\Gamma)}] \quad (28)$$

Figure 1 shows $v_{\text{TI}}(M_{\bullet})$ for different mass input parameters η , as well as the [η -independent] $\zeta > \zeta_c$ criterion, shown separately for cusp and core galaxies. Based on the Lauer et al. (2007) sample we take $r_{\text{inf}} = 25(8)M_{\bullet}^{0.6}$ pc and $r_b = 90M_{\bullet,8}^{0.5}$ (240 pc) and thus $r_b/r_{\text{inf}} \simeq 4M_{\bullet,8}^{-0.1}(30M_{\bullet,8}^{-0.6})$ for cores (cusps). We see that the for high η and low M_{\bullet} the $v_w \gtrsim v_{\text{TI}}$ criterion is more stringent, while for low η and high M_{\bullet} , the $\zeta > \zeta_c$ criterion is more stringent.

The minimum heating rate for thermal stability corresponds to the *maximum* thermally-stable inflow rate. From equations (27) and (28) this is

$$\frac{\dot{M}_{\text{TI}}}{\dot{M}_{\text{edd}}} \simeq \begin{cases} \min \begin{cases} 2 \times 10^{-4} \eta_{0.02}^{0.47} M_{\bullet,8}^{0.36} \\ 2 \times 10^{-5} \eta_{0.02} M_{\bullet,8}^{0.19} \end{cases} & \text{core,} \\ \min \begin{cases} 8 \times 10^{-5} \eta_{0.02}^{0.59} M_{\bullet,8}^{0.28} \\ 2 \times 10^{-5} \eta_{0.02} M_{\bullet,8}^{0.15} \end{cases} & \text{cusps.} \end{cases} \quad (29)$$

Note that since the SMBH accretion rate cannot exceed the large scale inflow rate, \dot{M}_{TI} also represents the maximum thermally stable accretion rate.

What we describe above as ‘‘thermal instability’’ may in practice simply indicate an abrupt transition from a steady inflow-outflow solution to a global cooling flow, as opposed a true thermal instability. In the former case the stagnation radius diverges to large radii, increasing the density in the inner parts of the flow, which increases cooling and creates a large inflow of cold gas towards the nucleus. A true thermal instability would likely result in a portion of the hot ISM condensing into cold clouds, a situation which may or may not be present in a cooling flow. In this paper we do not distinguish between these possibilities, although both are likely present at some level. Finally, note that if the CNM were to ‘‘regulate’’ itself to a state of local marginal thermal instability (as has previously been invoked on cluster scales; e.g., Voit et al. 2015), then equation (29) might naturally reflect the characteristic mass fall-out rate and concomitant star formation rate.

3.5 Angular Momentum

Our spherically symmetric model neglects the effects of angular momentum on the gas evolution. However, all galaxies possess some net rotation, resulting in centrifugal forces becoming important at some radius $r_{\text{circ}} = l_s^2/(GM_{\bullet})$. Here $l_s = \langle rV_{\phi} \rangle|_{r_s}$ is the stellar specific angular momentum near the stagnation radius, from which most of the accreted mass originates, where V_{ϕ} is the stellar azimuthal velocity.

Emsellem et al. (2007) use two-dimensional kinematic data to measure the ratio of ordered to random motion in a sample of early type galaxies, which they quantify at each galactic radius R by the parameter

$$\lambda_R \equiv \frac{\langle r|V| \rangle}{\langle R\sqrt{V^2 + \sigma^2} \rangle} \underset{R \ll r_{\text{inf}}}{\sim} \frac{V_{\phi}}{\sigma}, \quad (30)$$

where σ is the velocity dispersion and the brackets indicate a luminosity-weighted average. The circularization radius of the accretion flow can be written in terms of λ_R as

$$\frac{r_{\text{circ}}}{r_s} \approx \frac{r_s}{r_{\text{inf}}} \lambda_R^2 \lesssim \lambda_R^2, \quad (31)$$

where we have used the definition $r_{\text{inf}} \equiv GM_{\bullet}/\sigma_{\bullet}^2$ and in the second inequality have assumed that $r_s \lesssim r_{\text{inf}}$, a condition which is satisfied for the thermally-stable solutions of interest.

Emsellem et al. (2007) (their Fig. 2) find that λ_R is generally < 0.1 on radial scales < 10 per cent of the galaxy half-light radius and that λ_R decreases with decreasing R interior to this point. From equation (31) we thus conclude that $r_{\text{circ}} \lesssim 0.01r_s$. For the low inflow rates considered the gas ($\dot{M}/\dot{M}_{\text{Edd}} < 0.01$) would be unable to cool on a dynamical time and would likely drive equatorial and polar outflows (Li et al. 2013). Our model cannot capture such two dimensional structures, but would still be relevant for intermediate polar angles where the gas is inflowing.

4 NUMERICAL RESULTS

Our numerical results, summarized in Table 2, allow us to study a range of CNM properties and to assess the validity of the analytic estimates from the previous section.

Figure 2 shows profiles of the density $\rho(r)$, temperature

Table 2. Summary of Numerical Solutions

M_{\bullet} (M_{\odot})	v_w (km s^{-1})	$r_b^{(a)}$ (pc)	$r_s/r_{\text{inf}}^{(b)}$ -	$\left(\frac{\dot{M}}{\dot{M}_{\text{edd}}}\right)_{r_s}^{(c)}$ ($\eta = 0.2$) -	$\left(\frac{\dot{q}_{\text{heat}}}{ \dot{q}_{\text{rad}} }\right)_{r_s}^{(d)}$ ($\eta = 0.2$) -	Unstable η 's -
Cusp Galaxies, $\Gamma = 0.8$						
10^6	300	–	0.12	5.1×10^{-5}	28	0.6
...	600	–	3.2×10^{-2}	1.0×10^{-5}	1.9×10^3	
...	1200	–	7.9×10^{-3}	1.8×10^{-6}	7.7×10^4	
10^7	300	50	0.38	2.0×10^{-4}	4.5	0.2, 0.6
...	...	100	TI	TI	TI	
...	...	200	TI	TI	TI	
...	...	400	TI	TI	TI	
...	600	25	8.1×10^{-2}	3.2×10^{-5}	6.2×10^2	
...	...	100	8.1×10^{-2}	3.2×10^{-5}	6.2×10^2	
...	1200	100	2.0×10^{-2}	6.0×10^{-6}	2.6×10^4	
10^8	300	25	0.69	4.2×10^{-4}	5.5	0.6
...	...	50	0.92	6.0×10^{-4}	2	0.6
...	...	100	1.4	9.5×10^{-4}	0.48	0.2, 0.6
...	...	200	2.5	1.9×10^{-3}	5.3×10^{-2}	0.2, 0.6
...	450	100	0.43	2.4×10^{-4}	19	
...†	450	100	1.2	8.1×10^{-4}	2.6	
...	600	25	0.21	1.0×10^{-4}	2.1×10^2	
...	...	100	0.22	1.1×10^{-4}	1.7×10^2	
...†	...	100	0.22	1.1×10^{-4}	1.6×10^2	
...‡	...	100	0.07	2.8×10^{-5}	4.7×10^2	
...	...	200	0.23	1.1×10^{-4}	1.6×10^2	
...	...	400	0.23	1.1×10^{-4}	1.5×10^2	
...	1200	100	5.0×10^{-2}	1.8×10^{-5}	8.3×10^3	
Core Galaxies, $\Gamma = 0.1$						
10^6	600	25	TI	TI	TI	
...	1200	–	1.5×10^{-2}	2.3×10^{-7}	1.7×10^5	
10^7	600	25	0.19	2.9×10^{-5}	79	0.6
...	...	50	TI	TI	TI	
...	1200	25	3.9×10^{-2}	1.4×10^{-6}	2.9×10^4	
...	...	50	4.1×10^{-2}	1.5×10^{-6}	2.3×10^4	
10^8	600	25	0.27	5.7×10^{-5}	1.0×10^2	
...	...	50	0.46	1.5×10^{-4}	9.4	0.2, 0.6
...	1200	25	8.5×10^{-2}	6.1×10^{-6}	8.2×10^3	
...	...	50	9.2×10^{-2}	7.0×10^{-6}	6.0×10^3	
...	...	100	0.1	8.8×10^{-6}	3.8×10^3	
...	...	200	0.15	1.7×10^{-5}	8.0×10^2	

(^a) Break radius of stellar density profile. (^b) $r_{\text{inf}} = 14M_{\bullet}^{0.6}$ as fixed in our numerical runs. (^c) Inflow rate in Eddington units, normalized to a stellar mass input parameter $\eta = 0.2$. (^d) Ratio of wind heating rate to radiative cooling rate at the stagnation radius. †Calculated with radiative cooling included, assuming mass loss parameter $\eta = 0.2$. ‡Calculated with radiative cooling and conductivity included, assuming mass loss parameter $\eta = 0.2$ and conductivity saturation parameter $\phi = 0.1$. Solutions including radiative cooling were performed for cusp galaxies with $v_w = 300 \text{ km s}^{-1}$ and core galaxies with $v_w = 600 \text{ km s}^{-1}$ for $\eta = 0.02, 0.2, \text{ and } 0.6$. Values of η resulting in thermally unstable solutions are marked in the final column. Solutions found to be thermally unstable for all $\eta \geq 0.02$ are denoted as **TI**.

$T(r)$, and radial velocity $|v(r)|/c_s$, for the cusp ($\Gamma = 0.8$) solutions within our grid. As expected, the gas density increases towards the SMBH $\rho \propto r^{-\nu}$ with $\nu \simeq 1$, i.e. shallower than the $-3/2$ power law for Bondi accretion. This power law behavior does not extend through all radii, however, as the gas density profile has a break coincident with the location of the break in the stellar light profile ($r_b = 100 \text{ pc}$). The temperature profile is relatively flat at large radii, but increases as $\propto 1/r^k$ interior to the sphere of influence, where $k \lesssim 1$, somewhat shallower than expected for virialized gas within the black hole sphere of influence. The inwardly directed velocity increases towards the hole with a

profile that is somewhat steeper than the local free-fall velocity $v \propto v_{\text{ff}} \propto r^{-1/2}$. The flow near the stagnation radius is subsonic, but becomes supersonic at two critical points. The inner one at $r \simeq 0.1r_s$ is artificially imposed for numerical stability, although we have verified that moving the inner boundary has a small effect on the solution properties near the stagnation radius. The outer one is located near the break radius, $r \simeq r_b$ and is caused by the transition to a steeper stellar density profile exterior to the outer Nuker break radius.

Figure 3 shows our calculation of the stagnation radius r_s/r_{inf} as a function of the wind heating parameter

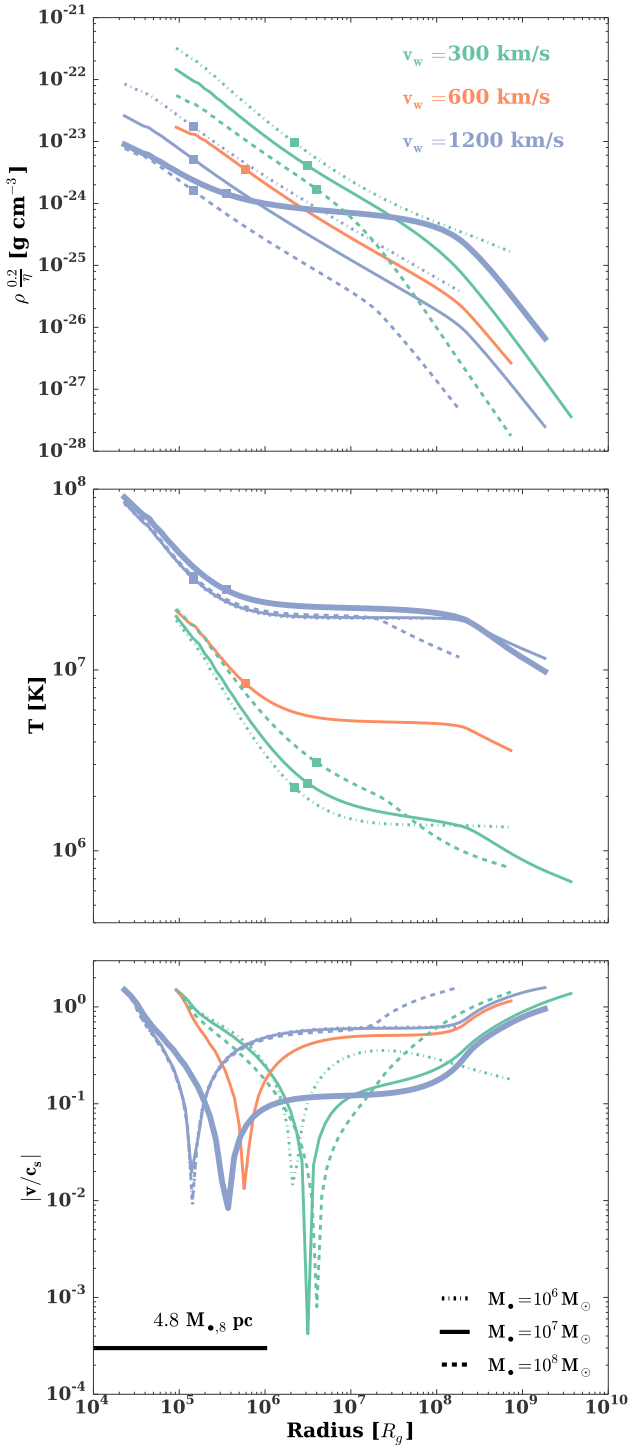


Figure 2. Radial profiles of the CNM density (*top*), temperature (*middle*), and velocity (*bottom*), calculated for a representative sample of galaxies. Colors denote values of the effective wind heating rate, $v_w = 1200 \text{ km s}^{-1}$ (blue), 600 km s^{-1} (orange), and 300 km s^{-1} (green). Line styles denote different black hole masses: $M_\bullet = 10^6 M_\odot$ (dot-dashed), $10^7 M_\odot$ (solid), and $10^8 M_\odot$ (dashed). Thin and thick lines denote cusp galaxies ($\Gamma=0.8$) and core galaxies ($\Gamma=0.1$), respectively. Squares mark the locations of the stagnation radius.

$\zeta = \sqrt{1 + (v_w/\sigma_0)^2}$, with different colors showing different values of v_w . Cusp and core galaxies are marked with square and triangles, respectively. Shown for comparison are our analytic results (eq. [A7]) with solid and dashed lines for cusp and core galaxies, respectively, calculated assuming $\nu = 1$ and $\nu = 0.6$, respectively.

Our analytic estimates accurately reproduce the numerical results in the high heating limit $\zeta \gg 1$ ($v_w \gg \sigma_0$; $r_s \lesssim r_{\text{inf}}$). However, for low heating the stagnation radius diverges above the analytic estimate, approaching the stellar break radius $r_b \gg r_{\text{inf}}$. This divergence occurs approximately when $\zeta < \zeta_c \propto (r_b/r_{\text{soi}})^{0.5(\Gamma-1)}$ (eq. [16]). Physically this occurs because the heating rate is insufficient to unbind the gas from the stellar potential. Thus, for small values of the heating rate (small ζ) the location of the stagnation radius will vary strongly with the break radius. This explains the behavior of the three vertically aligned green squares. These are three cusp ($\Gamma = 0.8$) galaxies with $M_\bullet = 10^8 M_\odot$ and $v_w = 300 \text{ km s}^{-1}$ but with different break radii ($r_b = 25, 50, \text{ and } 100 \text{ pc}$ from top to bottom). This divergence of the stagnation radius to large radii occurs at a higher value of ζ in core galaxies ($\Gamma = 0.1$), explaining the behavior of the two core galaxies shown in Fig. 3 as vertically aligned orange triangles.

Figure 4 shows the inflow rate for a sample of our numerical solutions for different values of $v_w = 300, 600$ and 1200 km s^{-1} , and for both core ($\Gamma=0.1$) and cusp galaxies ($\Gamma=0.8$). Shown for comparison is our simple analytic estimate of $\dot{M}/\dot{M}_{\text{edd}}$ from equation (18). For high wind velocities ($v_w \gg \sigma_0$) the stagnation radius lies well inside the black hole sphere of influence and our analytic estimate provides a good fit to the numerical results. However, for low wind velocities and/or high M_\bullet (large σ_0), the numerical accretion rate considerably exceeds the simple analytic estimate as the stagnation radius diverges to large radii (Fig. 3).

Fig. 5 shows the ratio of wind heating to radiative cooling, $\dot{q}_{\text{heat}}/|\dot{q}_{\text{rad}}|$ (eq. [25] and surrounding discussion) as a function of radius for $v_w = 300, 600$, and 1200 km s^{-1} , $M_\bullet = 10^7 M_\odot$, and $\Gamma = 0.8$. Radiative cooling is calculated using the cooling function of Draine (2011) for solar metallicity. For high heating rates of $v_w = 600$ and 1200 km s^{-1} cooling is unimportant across all radii, while for $v_w = 300 \text{ km s}^{-1}$ we see that $\dot{q}_{\text{heat}}/|\dot{q}_{\text{rad}}|$ and $t_{\text{cool}}/t_{\text{ff}}$ can be less than unity, depending on the wind mass loss parameter η . Because at the stagnation radius $\dot{q}_{\text{heat}}/|\dot{q}_{\text{rad}}|$ is within a factor of two of its minimum across the entire grid, the value of $(\dot{q}_{\text{heat}}/|\dot{q}_{\text{rad}}|)_{r_s}$ is a global diagnostic of thermal instability for cusp galaxies. For core galaxies, the minimum value for the ratio of wind heating to radiative cooling may be orders of magnitude less than the value at the stagnation radius. However, we find that the ζ/ζ_c criterion (see eq. (16)) combined with the ratio of wind heating to radiative cooling at r_s still gives a reasonable diagnostic of thermal stability for core galaxies.

Also note that for $v_w = 600$ and 1200 km s^{-1} we have $\dot{q}_{\text{heat}}/|\dot{q}_{\text{rad}}| \sim t_{\text{cool}}/t_{\text{ff}}$ near the stagnation radius, but these ratios diverge from each other at low heating ($v_w \lesssim 300 \text{ km s}^{-1}$). This results because equations (19), (20) underestimate the true gas density in the case of subsonic flow (weak heating).

Although most of our solutions neglect thermal conduction and radiative cooling, these effects are explored explic-

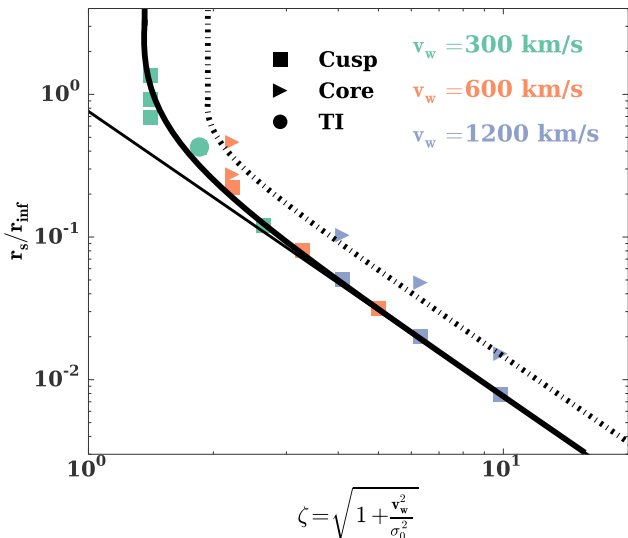


Figure 3. Stagnation radius r_s in units of the sphere of influence radius r_{inf} (eq. [3]) for galaxies in our sample as a function of the stellar wind heating parameter $\zeta \equiv \sqrt{1 + (v_w/\sigma_0)^2}$. Green, orange, and blue symbols correspond to different values of $v_w = 300, 600,$ and 1200 km s^{-1} , respectively. Squares correspond to cusp galaxies ($\Gamma = 0.8$), while triangles correspond to cores ($\Gamma = 0.1$). Green circles correspond to cusp solutions which would be thermally unstable. The black curves correspond to the analytic prediction from equation (A7), with thick solid and dot-dashed curves calculated for parameters ($\Gamma = 0.8, \nu \simeq 1$) and ($\Gamma = 0.1, \nu \simeq 0.6$), respectively. The thin black solid line corresponds to the simplified analytic result for r_s from equation (15) (recall that $r_{\text{inf}} \simeq GM_\bullet/\sigma_0^2$).

itly in a subset of simulations. Dagger symbols in Table 2 correspond to solutions for which we turned on radiative cooling. For cases which are far from being thermal instability when cooling is neglected (e.g., $M_\bullet = 10^8 M_\odot$, $v_w = 600 \text{ km s}^{-1}$, $r_b = 100 \text{ pc}$, $\eta = 0.2$, $\dot{q}_{\text{heat}}/|\dot{q}_{\text{rad}}| = 76$), including radiative cooling has little effect on the key properties of the solution, such as the stagnation radius, mass inflow rate, and the cooling ratio $\dot{q}_{\text{heat}}/|\dot{q}_{\text{rad}}|$. However, for solutions that are marginally thermally stable, including radiative losses acts to significantly decrease $\dot{q}_{\text{heat}}/|\dot{q}_{\text{rad}}|$. We calculated solutions with radiative cooling for all cusp galaxies with $v_w = 300 \text{ km s}^{-1}$ and for all core galaxies with $v_w = 600 \text{ km s}^{-1}$, each for three different values of $\eta = 0.02, 0.2, 0.6$, spanning the physical range of expected mass loss for continuous star formation (Fig. 7). Solutions found to be unstable for all values of η are marked in boldface as “TI” in Table 2, with the unstable values of η provided in the final column.

Including thermal conduction, by contrast, results in only order unity changes to our solutions for our fiducial value of the saturation parameter $\phi = 0.1$, consistent with our analytic expectations (eq. [23]). However, we found that for runs which included conductivity, the stagnation radius varied with the location of the inner grid boundary: as the boundary is moved inwards, more heat can be conducted outwards from deeper in the gravitational potential well of the black hole. We expect conductivity would begin to have a significant effect for an inner boundary $\lesssim 0.01 r_s$ (the conductive run in Table 2 has an inner grid boundary at

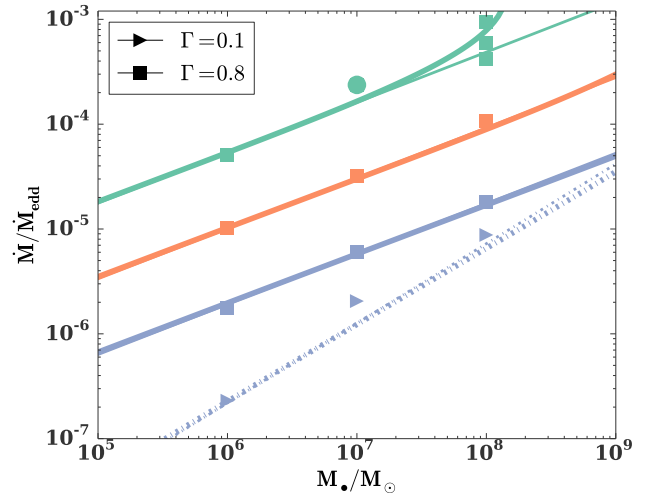


Figure 4. Inflow rate $\dot{M}/\dot{M}_{\text{edd}}$ versus SMBH mass for galaxies in our sample, calculated for different values of the wind heating parameter $v_w = 300 \text{ km s}^{-1}$ (green), 600 km s^{-1} (orange), and 1200 km s^{-1} (blue). Squares correspond to cusp galaxies ($\Gamma = 0.8$), while triangles correspond to cores ($\Gamma = 0.1$). The green circle corresponds to a cusp solution which would be thermally unstable. Thin solid and dot-dashed curves correspond to our simple analytic estimates of $\dot{M}/\dot{M}_{\text{edd}}$ (eq. [18]) for cusp and core galaxies, respectively. Thick curves correspond to the more accurate implicit analytic expression given by equation (A6).

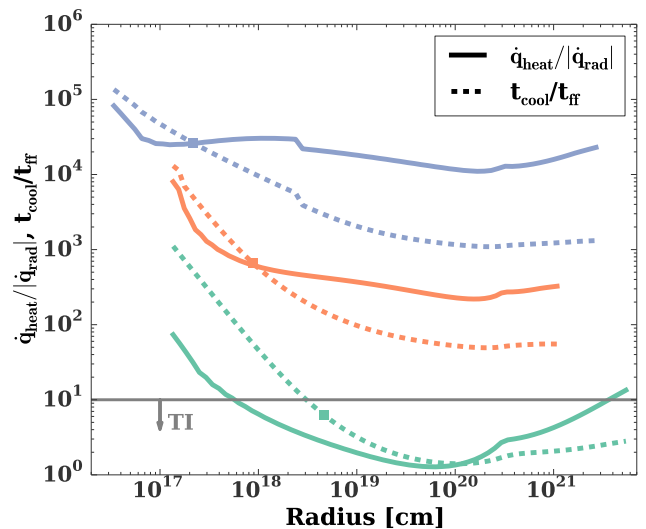


Figure 5. Ratio of the rates of heating to radiative cooling, $\dot{q}_{\text{heat}}/|\dot{q}_{\text{rad}}|$, as a function of radius (solid lines) for a $M_\bullet = 10^7 M_\odot$ cusp galaxy ($\Gamma = 0.8$). Dashed lines show the ratio of the cooling time-scale to the free-fall time-scale $t_{\text{cool}}/t_{\text{ff}}$. For high heating rates both ratios are approximately equal at the stagnation radius (squares). When $\dot{q}_{\text{heat}}/|\dot{q}_{\text{rad}}| \lesssim 10$ (or, equivalently, $t_{\text{cool}}/t_{\text{ff}} \lesssim 10$ near the stagnation radius), then the flow is susceptible to thermal instabilities.

$\sim 0.03r_s$). However, it is not clear physically if the magnetic field could remain coherent over so many decades in radius in the face of turbulence from stellar winds.

5 HEATING SOURCES

Key properties of the flow, such as the mass inflow rate and the likelihood of thermal instability, depend sensitively on the assumed heating rate $\propto qv_w^2$. In this section we estimate the heating rate, v_w , taking into account contribution from stellar winds, supernovae, millisecond pulsars and SMBH feedback. We make the simplifying assumption that all sources of energy injection are efficiently mixed into the bulk of CNM gas. In fact, slower stellar wind material may cool and form high density structures as in Cuadra et al. (2005). Additionally, some of the injected energy may leak away from the bulk of the CNM material through low density holes, as described by Harper-Clark & Murray (2009) for stellar feedback and by Zubovas & Nayakshin (2014) for AGN feedback.

We summarize the individual heating sources below, providing estimates of the value of the effective wind velocity

$$v_w = \sqrt{\frac{2t_h \dot{e}}{\eta \rho_*}} \quad (32)$$

for each, where \dot{e} is volumetric heating rate.

5.1 Stellar winds

Energy and mass input to the CNM by stellar winds is the sum of contributions from main sequence and post-main sequence populations. At early times following star formation, energy input is dominated by the fast line-driven outflows from massive stars (e.g., Voss et al. 2009). At later times energy input is dominated by main sequence winds (e.g., Naiman et al. 2013). Mass input is also dominated by the massive stars for very young stellar populations, but for most stellar ages the slow AGB winds of evolved low-mass stars dominate the mass budget.

In Appendix B we calculate the wind heating rate from stellar winds, v_w^* , and the mass loss parameter, η (eq. [8]), as a function of age, τ_* , of a stellar population which is formed impulsively (Fig. B1). At the earliest times ($\tau_* \lesssim 10^7$ yr), the wind heating rate exceeds 1000 km s^{-1} , while much later ($\tau_* \sim t_h$) stellar wind heating is dominated by main sequence winds is much lower, $v_w^* \sim 50 - 100 \text{ km s}^{-1}$. As will be shown in §5.5, for the case of quasi-continuous star formation representative of the average SFHs of low mass galaxies, the heating rate from stellar winds can also be significant, $v_w^* \sim 1000 \text{ km s}^{-1}$.

Stellar winds thus contribute a potentially important source of both energy and mass to the CNM. However, two additional uncertainties are (1) the efficiency with which massive stellar winds thermalize their energy and (2) heating from core collapse supernovae, which is potentially comparable to that provided by stellar winds. We neglect both effects, but expect they will act in different directions in changing the total heating rate.

5.2 Type Ia Supernovae

Type Ia SNe represent a source of heating, which unlike core collapse SNe is present even in an evolved stellar population. If each SN Ia injects thermal energy E_{Ia} into the interstellar medium, and the SN rate per stellar mass is given by R_{Ia} , then the resulting volumetric heating rate of $E_{\text{Ia}}R_{\text{Ia}}$ produces an effective heating parameter (eq. [32]) of

$$v_w^{\text{Ia}} = \sqrt{\frac{2t_h R_{\text{Ia}} E_{\text{Ia}}}{\eta}} \quad (33)$$

The thermal energy injected by each SN Ia, $E_{\text{Ia}} \simeq \epsilon_{\text{Ia}} 10^{51}$ erg, depends on the efficiency ϵ_{Ia} with which the initial blast wave energy is converted into bulk or turbulent motion instead of being lost to radiation. Thornton et al. (1998) estimate a radiative efficiency $\epsilon_{\text{Ia}} \sim 0.1$, depending weakly on surrounding density, but Sharma et al. (2014) argues that ϵ_{Ia} can be considerably higher, ~ 0.4 , if the SNe occur in a hot dilute medium, as may characterize the CNM. Hereafter we adopt $\epsilon_{\text{Ia}} = 0.4$ as fiducial.

The SN Ia rate, R_{Ia} , depends on the age of the stellar population, as it represent the convolution of the star formation rate and the Ia delay time distribution (DTD) divided by the present stellar mass. In the limit of impulsive star formation, R_{Ia} is the DTD evaluated at the time since the star formation episode. The observationally-inferred DTD (Fig. 1 of Maoz et al. 2012) has the approximate functional form

$$R_{\text{Ia}} = 1.7 \times 10^{-14} (\tau_*/t_h)^{-1.12} M_\odot^{-1} \text{ yr}^{-1} \quad (34)$$

where τ_* is the time since star formation.

From equations (33), (34) we thus estimate that

$$\begin{aligned} v_w^{\text{Ia}} &\approx 700(\epsilon_{\text{Ia}}/0.4)^{0.5} (\tau_*/t_h)^{-0.56} \eta_{0.02}^{-1/2} \text{ km s}^{-1} \\ &\approx 700(\epsilon_{\text{Ia}}/0.4)^{0.5} (\tau_*/t_h)^{0.09} \text{ km s}^{-1}, \end{aligned} \quad (35)$$

where the second line assumes $\eta \simeq 0.02(\tau_*/t_h)^{-1.3}$ for a single burst of star formation (e.g., Ciotti et al. 1991).

The high value of v_w^{Ia} implies that Ia SNe represent an important source of CNM heating. However, SNe can only be approximated as supplying heating which is spatially and temporally homogeneous if the rate of SNe is rapid compared to the characteristic evolution time of the flow at the radius of interest (Shcherbakov et al. 2014). We define the ‘‘Ia radius’’

$$r_{\text{Ia}} \sim \left(\frac{G}{R_{\text{Ia}} \sigma_0} \right)^{1/2} \sim 35 M_{\bullet,8}^{-0.1} (\tau_*/t_h)^{0.56} \text{ pc} \quad (36)$$

as the location exterior to which the time interval between subsequent supernovae $\tau_{\text{Ia}} \sim (M_{\text{enc}} R_{\text{Ia}})^{-1} \sim G/(r\sigma_0^2 R_{\text{Ia}})$ exceeds the local dynamical time-scale $t_{\text{dyn}} \sim r/\sigma_0$, where we again adopt the Ia rate for an old stellar population and in the final equality we estimate $\sigma_0 \approx \sqrt{3}\sigma_*$ using $M_\bullet - \sigma$ (eq. [4]).

Assuming that $v_w^{\text{Ia}} \gg \sigma_0$ then by substituting v_w^{Ia} (eq. 35) into equation (15) for the stagnation radius, we find that

$$\begin{aligned} \frac{r_{\text{Ia}}}{r_s} \Big|_{v_w^{\text{Ia}}} &\approx \begin{cases} 7 \eta_{0.02}^{-1} M_{\bullet,8}^{-1.1} (\epsilon_{\text{Ia}}/0.4) (\tau_*/t_h)^{-0.56} & \text{core} \\ 14 \eta_{0.02}^{-1} M_{\bullet,8}^{-1.1} (\epsilon_{\text{Ia}}/0.4) (\tau_*/t_h)^{-0.56} & \text{cusp} \end{cases} \\ &\approx \begin{cases} 7 M_{\bullet,8}^{-1.1} (\epsilon_{\text{Ia}}/0.4) (\tau_*/t_h)^{0.74} & \text{core} \\ 14 M_{\bullet,8}^{-1.1} (\epsilon_{\text{Ia}}/0.4) (\tau_*/t_h)^{0.74} & \text{cusp} \end{cases} \end{aligned} \quad (37)$$

SN Ia can only be approximated as a steady heating source near the stagnation radius for extremely massive SMBHs with $M_\bullet \gtrsim 10^9 M_\odot$ or for a very young stellar population with $\tau_\star \ll t_h$.

Even if SN Ia are rare near the stagnation radius, they may cap the inflow rate (and thus the SMBH accretion) rate by periodically blowing gas out of the nucleus of low mass galaxies. Between successive SNe, stars release a gaseous mass $M_g \approx \eta M_\star \tau_{\text{Ia}}/t_h$ interior to the Ia radius, which is locally gravitationally bound to the SMBH by an energy $E_{\text{bind}} \gtrsim M_g \sigma_0^2$. From the above definitions it follows that

$$\frac{E_{\text{Ia}}}{E_{\text{bind}}} \lesssim \frac{(v_w^{\text{Ia}})^2}{2\sigma_0^2}. \quad (38)$$

Hence, for low mass BHs with $\sigma_0 \ll v_w^{\text{Ia}}$, SN Ia are capable of dynamically clearing out gas from radii $\sim r_{\text{Ia}} \gtrsim r_s$. Thus even when heating is sufficiently weak that the stagnation radius formally exceeds r_{Ia} , the SMBH accretion rate is still limited to a value

$$\frac{\dot{M}_{\text{Ia}}}{\dot{M}_{\text{edd}}} \approx \frac{\eta M_\bullet}{\dot{M}_{\text{edd}} t_h} \left(\frac{r_{\text{Ia}}}{r_{\text{inf}}} \right)^{2-\Gamma} \approx \begin{cases} 4.5 \times 10^{-4} M_{\bullet,8}^{-1.33} (\tau_\star/t_h)^{-0.2} & \text{core} \\ 2.2 \times 10^{-4} M_{\bullet,8}^{-0.84} (\tau_\star/t_h)^{-0.6} & \text{cusp,} \end{cases} \quad (39)$$

obtained substituting the Ia radius r_{Ia} (eq. [36]) for r_s in the derivation leading to our estimate of \dot{M} (eq. [18]).

The deep gravitational potential wells of high mass galaxies prevent SN Ia from dynamically clearing out gas in these systems ($\sigma_0 \gg v_w^{\text{Ia}}$). Equation (39) nevertheless still represents a cap on the accretion rate in practice because the Ia heating rate (eq. [35]) is usually high enough to prevent the stagnation radius (calculated including the Ia heating) from substantially exceeding r_{Ia} . If the stagnation radius moves inwards from r_{Ia} , then decreased heating will force it outwards again. On the other hand, if the stagnation radius moves well outside of r_{Ia} , then the high level of Ia heating will force it inwards.

5.3 Millisecond Pulsars

Energy injection from the magnetic braking of millisecond pulsars (MSPs) is a potentially important heating source. If the number of MSPs per unit stellar mass is n_{mSP} and each contributes on average a spin-down luminosity \bar{L}_{sd} , then the resulting heating per unit volume $\dot{e} \approx \bar{L}_{\text{sd}} n_{\text{mSP}} \epsilon_{\text{mSP}}$ results in an effective heating rate (eq. [32]) of

$$v_w^{\text{MSP}} \sim 30 \left(\frac{\epsilon_{\text{mSP}}}{0.1} \right)^{1/2} \left(\frac{\bar{L}_{\text{sd}}}{10^{34} \text{ erg s}^{-1}} \right)^{1/2} \eta_{0.02}^{-1/2} \text{ km s}^{-1}, \quad (40)$$

where ϵ_{mSP} is the thermalization efficiency of the wind, normalized to a value $\lesssim 0.1$ based on that inferred by modeling the interstellar media of globular clusters (Naiman et al. 2013). Our numerical estimate assumes a pulsar density $n_{\text{mSP}} \sim 3 \times 10^{-40} \text{ MSPs g}^{-1}$, calculated from the estimated $\sim 30,000$ MSPs in the Milky Way (Lorimer 2013) of stellar mass $\approx 6 \times 10^{10} M_\odot$.

Based on the ATNF radio pulsar catalog (Manchester et al. 2005), we estimate the average spin-down luminosity of millisecond pulsars in the field to be $\bar{L}_{\text{sd}} \sim 10^{34} \text{ erg s}^{-1}$, resulting in $v_w^{\text{MSP}} \lesssim 30 \text{ km s}^{-1}$ for $\eta \gtrsim 0.02$. For higher

spin-down luminosities, $L_{\text{sd}} \simeq 10^{35} \text{ ergs s}^{-1}$ characteristic of some Fermi-detected pulsars, then the higher value of $v_w^{\text{MSP}} \lesssim 300 \text{ km s}^{-1}$ makes MSP heating in principle important under the most optimistic assumptions $\epsilon_{\text{mSP}} = 1$ and $\eta = 0.02$.

5.4 SMBH Feedback

Feedback from accretion onto the SMBH represents an important source of heating which, however, is also the most difficult to quantify (e.g., Brighenti & Mathews 2003, Di Matteo et al. 2005; Kurosawa & Proga 2009; Fabian 2012 for a recent review). A key difference between AGN heating and the other sources discussed thus far is its dependence on the SMBH accretion rate \dot{M}_\bullet , which is itself a function of the heating rate (eq. [17]).

5.4.1 Compton Heating

There are two types of SMBH feedback: kinetic and radiative. Radiative feedback is potentially effective even in low luminosity AGN via Compton heating (e.g., Sazonov et al. 2004, Ciotti et al. 2010), which provides a volumetric heating rate (Gan et al. 2014)

$$\dot{e} = 4.1 \times 10^{-35} n^2 \xi T_C \text{ erg cm}^{-3} \text{ s}^{-1}, \quad (41)$$

where $\xi = L/nr^2$ is the ionization parameter and L is the SMBH luminosity with Compton temperature $T_C \sim 10^9 \text{ K} \gg T$ (e.g., Ho 1999, Eracleous et al. 2010).

The importance of Compton heating can be estimated by assuming the SMBH radiates with a luminosity $L = \epsilon \dot{M} c^2$, where ϵ is the radiative efficiency and where \dot{M} is estimated from equation (17). Then using equations (15), (17), (20), (24) we calculate from equation (32) that the effective heating rate at the stagnation radius is given by

$$v_w^{\text{C}} \simeq \begin{cases} 24 \eta_{0.02}^{0.5} T_{C,9}^{0.5} \epsilon_{-2}^{0.5} M_{\bullet,8}^{0.38} v_{500}^{-1.4} \text{ km s}^{-1} & , \text{core} \\ 30 \eta_{0.02}^{0.5} T_{C,9}^{0.5} \epsilon_{-2}^{0.5} M_{\bullet,8}^{0.24} v_{500}^{-0.7} \text{ km s}^{-1} & , \text{cusp,} \end{cases} \quad (42)$$

where $T_{C,9} = T_C/10^9 \text{ K}$ and $\epsilon_{-2} = \epsilon/0.01 \sim 1$. We caveat that, unlike stellar wind heating, Compton heating depends on radius, scaling as $v_w^{\text{C}}(r) \propto (n^2 \xi / \rho_\star)^{1/2} \propto r^{(\Gamma-\nu-1)/2}$, i.e. $\propto r^{-0.6}$ and $\propto r^{-0.75}$ for core ($\Gamma = 0.8$; $\nu \simeq 1$) and cusp ($\Gamma = 0.1$; $\nu \simeq 0.6$) galaxies, respectively. Although our model's assumption that the heating parameter be radially constant is not satisfied, this variation is sufficiently weak that it should not significantly alter our conclusions.

If Compton heating acts alone, i.e. $\tilde{v}_w = v_w^{\text{C}}$, then solving equation (42) for \tilde{v}_w yields

$$v_w^{\text{C}} \simeq \begin{cases} 140 \eta_{0.02}^{0.21} T_{C,9}^{0.21} \epsilon_{-2}^{0.21} M_{\bullet,8}^{0.16} \text{ km s}^{-1} & , \text{core} \\ 95 \eta_{0.02}^{0.34} T_{C,9}^{0.29} \epsilon_{-2}^{0.29} M_{\bullet,8}^{0.14} \text{ km s}^{-1} & , \text{cusp.} \end{cases} \quad (43)$$

Compton heating is thus significant in young stellar populations with relatively high mass loss rates, e.g. $v_w^{\text{C}} \gtrsim 300 \text{ km s}^{-1}$ for $\eta \gtrsim 1$.

The inflow rate corresponding to a state in which Compton heating self-regulates the accretion flow is given by substituting equation (43) into equation (18):

$$\frac{\dot{M}_C}{\dot{M}_{\text{edd}}} \approx \begin{cases} 2 \times 10^{-3} \eta_{0.02}^{0.2} T_{C,9}^{-0.8} \epsilon_{-2}^{-0.8} M_{\bullet,8}^{0.16} & , \text{core} \\ 8 \times 10^{-4} \eta_{0.02}^{0.3} T_{C,9}^{-0.7} \epsilon_{-2}^{-0.7} M_{\bullet,8}^{0.14} & , \text{cusp.} \end{cases} \quad (44)$$

Sharma et al. (2007) estimate the value of the radiative efficiency of low luminosity AGN, ϵ_{rad} , based on MHD shearing box simulations of collisionless plasmas. For Eddington ratios of relevance, their results (shown in their Fig. 6) are well approximated by

$$\epsilon_{\text{rad}} \simeq \begin{cases} 0.03 \left(\frac{\dot{M}_\bullet}{10^{-4} \dot{M}_{\text{edd}}} \right)^{0.9} & \frac{\dot{M}_\bullet}{\dot{M}_{\text{edd}}} \lesssim 10^{-4} \\ 0.03 & 10^{-2} \gtrsim \frac{\dot{M}_\bullet}{\dot{M}_{\text{edd}}} \gtrsim 10^{-4}, \end{cases} \quad (45)$$

where \dot{M}_\bullet is the BH accretion rate. In general \dot{M}_\bullet will be smaller than the inflow rate \dot{M} calculated thus far by a factor $\alpha < 1$ due to outflows from the accretion disc on small scales. Thus, the full efficiency relating the mass inflow rate to the radiative output is $\epsilon = \alpha \epsilon_{\text{rad}}$, where we take $\alpha = 0.1$ following Li et al. (2013), who find that the fraction of the inflowing matter lost to outflows equals the Shakura-Sunyaev viscosity parameter of the disc.

Substituting ϵ into equation (44) and solving for the inflow rate results in

$$\frac{\dot{M}_C}{\dot{M}_{\text{edd}}} \approx \begin{cases} 4 \times 10^{-2} \eta_{0.02}^{0.2} T_{C,9}^{-0.8} M_{\bullet,8}^{0.16} & , \text{core} \\ 9 \times 10^{-3} \eta_{0.02}^{0.3} T_{C,9}^{-0.7} M_{\bullet,8}^{0.14} & , \text{cusp.} \end{cases} \quad (46)$$

Accretion may not be truly steady in cases where AGN heating dominates, due to the inherent delay between black hole feedback and the structure of the accretion flow on larger scales. Equation (46) may nevertheless represent a characteristic average value for the inflow rate if a quasi-equilibrium is achieved over many cycles.

5.4.2 Kinetic Feedback

Kinetic feedback results from outflows of energy or momentum from close to the black hole in the form of a disc wind or jet, which deposits its energy as heat, e.g. via shocks or wave dissipation, over much larger radial scales (e.g. McNamara & Nulsen 2007; Novak et al. 2011; Gaspari et al. 2012a).

Assume that the outflow power is proportional to the SMBH accretion rate, $L_j = \epsilon_j \dot{M}_\bullet c^2 = 0.1 \epsilon_j \dot{M} c^2$, where $\epsilon_j < 1$ is an outflow efficiency factor and we have again assumed a fraction $\alpha = 0.1$ of the infall rate reaches the SMBH. Further assume that this energy is deposited as heat uniformly interior to a radius r_{heat} and volume $V_{\text{heat}} \propto r_{\text{heat}}^3$. The resulting volumetric heating rate $e = 0.1 \epsilon_j \dot{M} c^2 / V_{\text{heat}}$ near the stagnation radius results in a heating parameter given by

$$v_w^\bullet \approx \left(\frac{0.2 t_{\text{h}} \epsilon_j \dot{M} c^2}{V_{\text{heat}} \eta \rho_\star |_{r_s}} \right)^{1/2} \quad (47)$$

$$\approx \frac{700}{\sqrt{2-\Gamma}} \text{ km s}^{-1} \left(\frac{\epsilon_j}{10^{-5}} \right)^{1/2} \left(\frac{r_s}{r_{\text{heat}}} \right)^{3/2}, \quad (48)$$

where we have used the facts that $\dot{M} = \eta M_\star |_{r_s} / t_{\text{h}}$ and $\rho_\star(r_s) = M_\star(r_s)(2-\Gamma)/(4\pi r_s^3)$. If the bulk of the energy from kinetic feedback is released near the stagnation radius, then even a small heating efficiency $\epsilon_j \gtrsim 10^{-4}$ is sufficient for v_w^\bullet to exceed other sources of non-accretion powered heating. However, if this energy is instead deposited over much larger physical scales comparable to the size of the galaxy, i.e. $r_{\text{heat}} \gtrsim 10 \text{ kpc} \sim 10^4 r_s$, then kinetic feedback is unimportant, even for a powerful outflow with $\epsilon_j \sim 0.1$.

The time required for a jet of luminosity L_j and half

opening angle $\theta_j = 0.1$ (characteristic of AGN jets) to propagate through a gaseous mass M_g of radius r is estimated from Bromberg et al. (2011) to be

$$t_{\text{jet}} \sim 4000 \text{ yr} \left(\frac{L_j}{10^{40} \text{ erg s}^{-1}} \right)^{-1/3} \left(\frac{r}{\text{pc}} \right)^{2/3} \left(\frac{M_g}{10^8 M_\odot} \right)^{1/3} \quad (49)$$

Approximating $M_g \sim \dot{M} t_{\text{ff}}$, the ratio of the jet escape time-scale to the dynamical time-scale $t_{\text{dyn}} \sim r/\sigma$ is given by

$$\frac{t_{\text{jet}}}{t_{\text{dyn}}} \sim 7 \times 10^{-3} M_{\bullet,8}^{0.13} \left(\frac{\epsilon_j}{10^{-6}} \right)^{-1/3}, \quad (50)$$

independent of r . A jet with power sufficient to appreciably heat the CNM on radial scales $\sim r_s$ ($\epsilon_j \gtrsim 10^{-5}$) also necessarily has sufficient power to escape the nuclear region and propagate to much larger radii. Slower outflows from the accretion disc, instead of a collimated relativistic jet, provide a potentially more promising source of feedback in these systems.

As in the case of Compton heating, kinetic heating could in principle ‘self-regulate’ the accretion flow insofar as a lower heating rate results in a higher accretion rate (eq. [48]), which in turn may create stronger kinetic feedback. However, given the uncertainty in the efficiency of kinetic heating, we hereafter neglect its effect and defer further discussion to §6.6.

5.5 Combined Heating Rate

The total external gas heating rate,

$$v_w = \sqrt{(v_w^\star)^2 + (v_w^{\text{MSP}})^2 + (v_w^{\text{Ia}})^2 + (v_w^\bullet)^2}, \quad (51)$$

includes contributions from stellar winds, supernovae, pulsars, and radiative SMBH feedback. We implicitly assume the different sources of energy injection mix efficiently. In reality, this may not be the case as slower velocity sources cool and form high density structure due to high pressure from the environment (Cuadra et al. 2005).

The strength of each heating source depends explicitly on the SMBH mass and the stellar population in the galactic nuclear region. The latter could best be described by a single starburst episode in the past, or by a more continuous SFH that itself varies systematically with the galaxy mass and hence M_\bullet .

5.5.1 Single Starburst

Figure 6 shows the contributions of heating sources as a function of time τ_\star after a burst of star formation for black holes of mass $M_\bullet = 10^6 M_\odot$ (top) and $M_\bullet = 10^8 M_\odot$ (bottom). The heating and mass input parameters due to stellar winds, $v_w^\star(\tau_\star)$ and $\eta(\tau_\star)$, are calculated as described in Appendix B (Fig. B1). The SN Ia and Compton heating rates, v_w^{Ia} and v_w^{C} , are calculated from equations (35) and (42), respectively, which also make use of $\eta(\tau_\star)$ as set by stellar winds.⁶ SN Ia heating depends also on a convolution of the DTD (eq. [34]) and the SFH, which reduces to the DTD itself

⁶ Both v_w^{C} and v_w^{Ia} (through r_s/r_{Ia}) depend on the total heating rate (eq. [51]), requiring us to simultaneously solve a series of implicit equations to determine each.

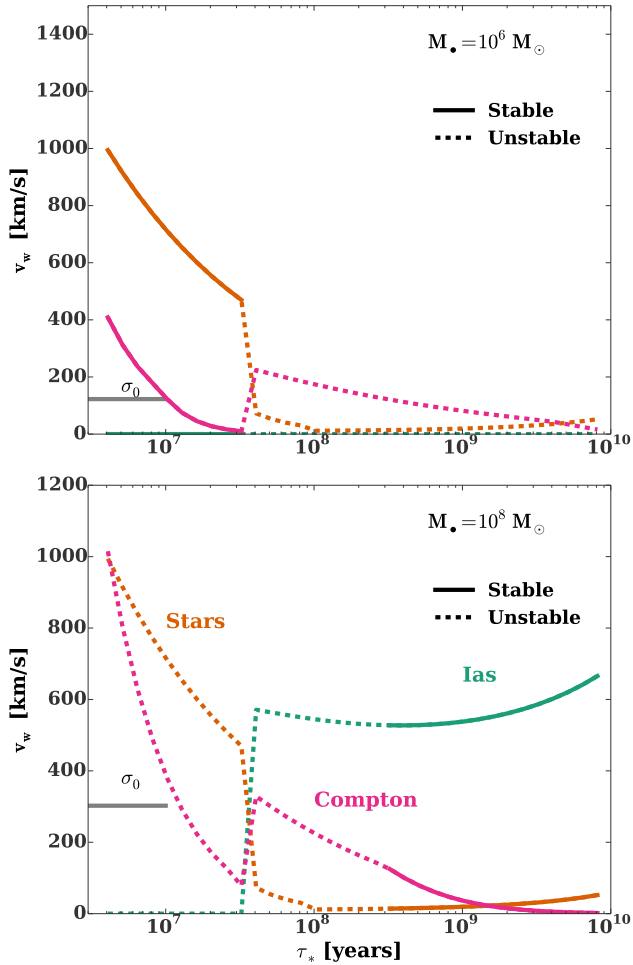


Figure 6. Sources contributing to the gas heating rate at time τ_* after a single burst of star formation. Top and bottom panels show black hole masses of $M_\bullet = 10^6 M_\odot$ and $M_\bullet = 10^8 M_\odot$ (both cusps with $\Gamma = 0.8$). Solid and dashed lines show the ranges of τ_* for which the accretion flow is thermally stable and unstable, respectively, according to the ratio of $\dot{q}_{\text{heat}}/|\dot{q}_{\text{rad}}|$ near the stagnation radius (eq. [25]). Shown with horizontal gray lines are the stellar velocity dispersion for each SMBH mass, estimated as $\sigma_0 = \sqrt{3}\sigma_\bullet$ (eq. [4]).

for a single star burst. We account for the expected suppression of SN Ia heating resulting from its non-steady nature by setting $v_w^{\text{Ia}} = 0$ when the stagnation radius (calculated *excluding* Ia heating) exceeds the Ia radius r_{Ia} (eq. [36]).

Figure 6 shows that stellar winds are the most important heating source at early times, $\tau_* \lesssim 10^7$ years. Compton heating becomes more important at later times due to (1) the higher accretion rates that accompany the overall decrease in all sources of heating, coupled with (2) the persistently high mass loss rates and gas densities associated with the still relatively young stellar population. Interestingly, for $M_\bullet = 10^6 M_\odot$, there are two consistent solutions for times $10^8 \text{ yr} \lesssim \tau_* \lesssim 10^9 \text{ yr}$: one which has high Ia heating and low compton heating and one with low Ia heating and high compton heating. We choose the latter, but our model cannot truly distinguish between these scenarios. Also, neither scenario would produce a thermally stable flow. For high-

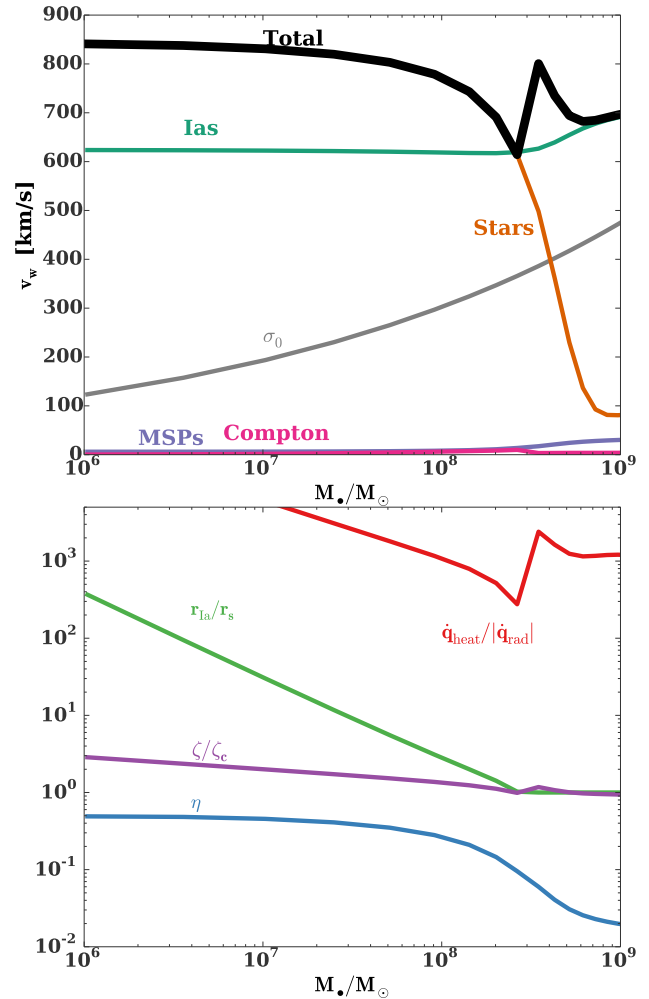


Figure 7. *Top Panel:* Sources contributing to the total heating rate of the CNM, v_w (black): stellar wind heating (orange), Ia supernovae (green), millisecond pulsars (blue), and compton heating (pink). Each heating source varies with black hole mass M_\bullet calculated for average SFHs from [Moster et al. \(2013\)](#); see Appendix B for details. *Bottom Panel:* The ratio of the total heating rate ($\dot{q}_{\text{heat}} \propto v_w^2$) from the top panel to the radiative cooling rate ($|\dot{q}_{\text{rad}}|$) at the stagnation radius (red), parameter η characterizing stellar mass loss rate (eq. [8]) as a function of black hole mass M_\bullet , calculated for average star SFHs from [Moster et al. 2013](#) (blue), the ratio of Ia radius to stagnation radius as a function of M_\bullet (green), and the ratio of ζ/ζ_c (purple), where ζ_c (eq. [16]) is the critical heating parameter $\zeta \equiv \sqrt{1 + (v_w/\sigma_0)^2}$ below which outflows are impossible. All quantities are calculated for core ($\Gamma = 0.1$) galaxies. The results for cusp galaxies are qualitatively similar.

mass black holes (Fig. 6, bottom panel), SN Ia dominate at all times after 10^7 yr. Both Type Ia and Type II supernovae could be an important heating source for times $\tau_* \leq 40$ Myr, albeit a non-steady one for $M_\bullet \lesssim 10^8 M_\odot$. For simplicity we neglect supernova heating for $\tau_* \leq 40$, keeping in mind that it could raise the overall heating by a factor of a few.

As the total heating rate declines with time, the flow inevitably becomes thermally unstable according to the criterion $(\dot{q}_{\text{heat}}/|\dot{q}_{\text{rad}}|)_{r_s} \lesssim 10$ (eq. [27]), as shown by dashed lines in Fig. 6. Compton heating is neglected in calculat-

ing thermal stability because—unlike local stellar feedback mechanisms—it is not clear that SMBH feedback is capable of stabilizing the flow given its inability to respond instantaneously to local changes in gas properties. Thermally unstable flow is present throughout the single starburst case except at very early times, $\tau_* \lesssim 10^7$ yr and at late times $\tau_* \gtrsim 10^9$ yr in the high M_\bullet case.

Finally, MSP heating is negligibly small for fiducial parameters and hence is not shown, while kinetic feedback is neglected given its uncertain efficiency (§6.6).

5.5.2 Continuous SFH

A single burst of star formation does not describe the typical star formation history of most galaxies. Qualitatively, smaller galaxies will on average experience more recent star formation, resulting in energetic young stellar winds and supernovae which dominate the gas heating budget. Massive galaxies, on the other hand, will on average possess older stellar populations, with their heating rates dominated by SN Ia (on large radial scales) and SMBH feedback. We estimate the average value of v_w as a function of SMBH mass for each heating source by calculating its value using the average cosmic star formation histories of [Moster et al. \(2013\)](#). Appendix B describes how the average SFH is used to determine the stellar wind heating v_w^* and mass return parameter η as a function of M_\bullet (Fig. 7; top panel). SFHs are also convolved with the Ia DTD distribution to determine the SN Ia heating.

Figure 7 shows $v_w(M_\bullet)$ from each heating source (stars, MSPs, SNe Ia, and black hole feedback) calculated for the average SFH of galaxies containing a given black hole mass. The younger stellar populations characterizing low mass galaxies with $M_\bullet \lesssim 3 \times 10^8 M_\odot$ are dominated by stellar winds, with $v_w^* \gtrsim 700$ km s⁻¹. Only for $M_\bullet \gtrsim 3 \times 10^8 M_\odot$ does the lack of young stellar populations significantly reduce the role of stellar wind heating. For these massive galaxies, however, the Ia radius is sufficiently small that SN Ia contribute a comparable level of heating, $v_w^{\text{Ia}} \gtrsim 500$ km s⁻¹ (SN Ia do not contribute to the heating in low mass galaxies because $r_{\text{Ia}} > r_s$; bottom panel).

Strikingly, we find that galactic nuclei that experience the same average SFH as their host galaxies possess thermally stable flows across all black hole masses. An important caveat, however, is that \tilde{v}_w is generally only a few times higher than the stellar velocity dispersion, i.e. $\zeta \sim \zeta_c$ (eq. [16]). This implies that the true stagnation radius and the inflow rate could be larger than our analytic estimates, potentially resulting in thermal instability in a significant fraction of galaxies. The bottom panel of Figure 7 also shows ζ/ζ_c , where ζ_c is estimated using fits for r_b , r_{inf} , and Γ derived from the [Lauer et al. \(2007\)](#) sample. In other words, the CNM of a significant fraction of massive ellipticals may be thermally unstable, not necessarily because they are receiving lower stellar feedback than the average for their galaxy mass, but due to the high heating required for stability given the structure of their stellar potential.

Realistic variations (“burstiness”) in the SFH can also produce lower stellar wind heating rates (Appendix B). Figure B2 shows the heating rate as a function of average black hole mass for non-fiducial cases in which the current ($z = 0$)

star formation is suppressed by a factor ι from its average $z = 0$ value, for a characteristic time-scale δt_* . For $\delta t_* \lesssim 10^7$ yr, we see that v_w^* is reduced by at most a factor of ≈ 2 from its average value, even for huge drops in the star formation rate ($\iota \sim 10^{-3}$). However, burstiness in the SFH over longer time-scales can suppress heating more significantly. When $\delta t_* \gtrsim 10^8$ yr, v_w^* becomes very sensitive to ι : at $\iota = 0.1$, $v_w^* \approx 400$ km s⁻¹ in most galaxies, but for smaller ι , $v_w^* \approx 200$ km s⁻¹ (an exception to this is in galactic nuclei with $M_\bullet \gtrsim 10^8 M_\odot$, where heating is stabilized by SN Ia). Our use of average cosmic SFHs is appropriate provided local variations are either on short time-scales ($\delta t_* \lesssim 10^7$ yr), or limited in magnitude ($\iota \gtrsim 0.1$). If both of these conditions are violated, then the effective heating rates for all but the most massive galaxies (where Ia explosions dominate) will fall by a factor $\gtrsim 4$ from our fiducial volumetric averages, calculated using SFHs from [Moster et al. \(2013\)](#).

Another potential complication is the discreteness of local sources. We assume heating and mass injection are smooth, but energy and mass injection may be dominated by a handful of stars, particularly for small M_\bullet . For example, for $M_\bullet \lesssim 10^8 M_\odot$, O stars dominate the energy injection in the average star formation histories of [Moster et al. \(2013\)](#), but the expected number of O stars inside the stagnation radius is 0.01 for $M_\bullet = 10^6 M_\odot$ and only exceeds 1 for $M_\bullet \gtrsim 10^7 M_\odot$, assuming circular stellar orbits⁷.

6 IMPLICATIONS AND DISCUSSION

6.1 Inflow and Black Hole Accretion Rates

Figure 7 shows that the heating associated with the average SFH of a galaxy is approximately constant with SMBH mass, except for the largest black holes with $M_\bullet \gtrsim 5 \times 10^8 M_\odot$. For a fixed wind heating parameter, the Eddington ratio $\dot{M}/\dot{M}_{\text{edd}}$ increases $\propto M_\bullet^{0.5(0.8)}$ for core(cusp) galaxies, respectively (Fig. 4; eq. [18]).

Figure 8 (top panel) shows with solid lines the inflow rate as a function of black hole mass for the average star formation heating, calculated from equation (18) using our results for the total wind heating (Fig. 4). This average inflow rate increases from $\dot{M} \sim 10^{-6} - 10^{-5} M_\odot \text{ yr}^{-1}$ for low-mass black holes ($M_\bullet \sim 10^6 M_\odot$) to $\dot{M} \sim 10^{-4} M_\odot \text{ yr}^{-1}$ for $M_\bullet \sim 10^8 M_\odot$. These fall below the maximum thermally stable inflow rate, \dot{M}_{TI} (yellow lines).

For low mass black holes, blow out from SN Ia caps the SMBH accretion rate at a value $\dot{M}_{\text{Ia}} \sim 10^{-6} - 10^{-5} M_\odot \text{ yr}^{-1}$ (green lines; eq. [39]), which is however not low enough to prevent otherwise thermally-unstable flow at smaller radii. For higher M_\bullet the stagnation radius resides close to the Ia radius so Ia heating contributes to the steady gas heating rate, even if the energy released by a single Ia is insufficient to unbind gas from the stellar bulge (eq. [38]). This explains why the black and teal lines meet at high M_\bullet .

Shown also for comparison in Figure 8 (top panel) is the inflow rate, \dot{M} , onto SgrA* calculated by [Quataert \(2004\)](#) and by [Cuadra et al. \(2008\)](#). Also shown is the range of \dot{M}

⁷ If the stars providing the heating reside on elliptical orbits, a greater number will contribute at any time due to the portion of their orbital phase spent at small radii.

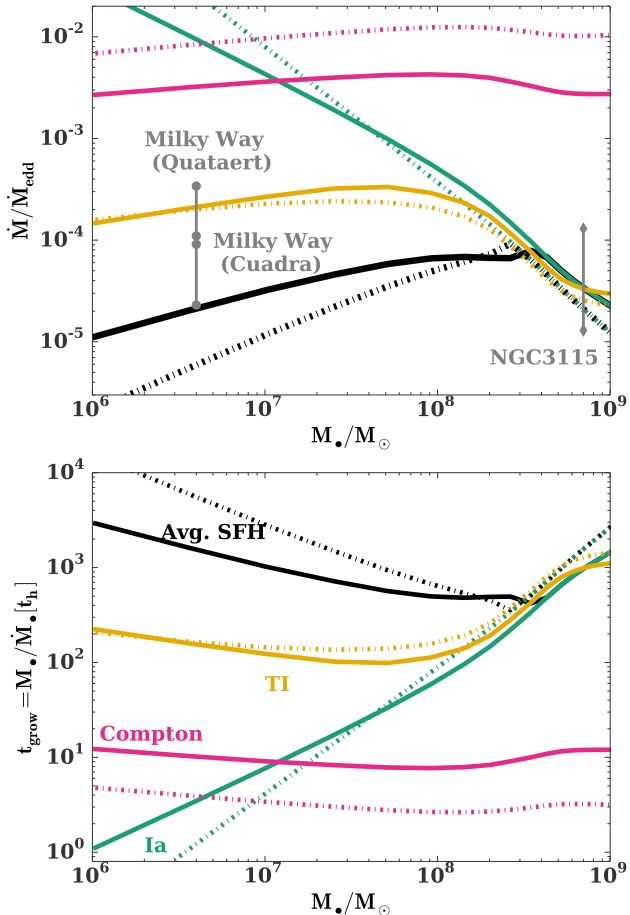


Figure 8. *Top panel:* Gas inflow rate $\dot{M}/\dot{M}_{\text{Edd}}$ as a function of black hole mass M_{\bullet} , shown for core ($\Gamma = 0.1$, dot-dashed) and cusp galaxies ($\Gamma = 0.8$, solid). Black lines show the inflow rate calculated from equation (18) using the heating rate provided at $z = 0$ by the average star formation histories for each galaxy mass (Fig. 7). Teal lines show the maximum accretion set by Ia supernovae blow-out or heating, \dot{M}_{Ia} (39). Red lines show the inflow rate obtained if Compton heating acts alone, \dot{M}_{C} (eq. [46]). Yellow lines show the maximum inflow rate for a thermally stable flow near the stagnation radius, \dot{M}_{TI} (eq. [29]). Also shown are the inferred inflow rates of SgrA* from Quataert (2004) and Cuadra et al. (2008) (gray circles) and for NGC3115 from Shcherbakov et al. (2014) (gray diamonds). *Bottom panel:* Growth times $t_{\text{grow}} \equiv M_{\bullet}/\dot{M}_{\bullet}$ in units of the Hubble time t_{h} for each of the accretion rates shown in the top panel, where $\dot{M}_{\bullet} = \alpha\dot{M}$, where $\alpha = 0.1$, to account for the fraction of inflowing mass lost to disc outflows on small scales.

for the low-luminosity AGN NGC3115 derived through detailed modeling by Shcherbakov et al. (2014), who find a range of inflow rates depending on the assumed model for thermal conductivity. The inflow rate SgrA* estimated from Quataert (2004)⁸ exceeds our estimate of \dot{M} due to the average SFH for the same M_{\bullet} by at least an order of magnitude. This is because the mass source term in Quataert (2004) ex-

⁸ There is a typo in Quataert (2004): the inflow rate corresponds total stellar mass loss rate of $5 \times 10^{-4} M_{\odot} \text{ yr}^{-1}$ not $10^{-3} M_{\odot} \text{ yr}^{-1}$, as pointed out by Cuadra et al. (2006).

ceeds ours by a factor of ~ 50 (for cusp galaxies). The star formation in the central parsec of the Milky Way cannot be described as steady-state: feedback is instead dominated by the stellar winds from the ring of young massive stars of mass $\sim 10^4 M_{\odot}$ and estimated age ~ 10 Myr (e.g., Schödel et al. 2007). Such a star formation history is better described by our impulsive (starburst) scenario, for which the value of $\eta \sim 30$ at $\tau_{\star} = 10^7$ yr (Fig. B1) is a factor of ~ 100 times higher than the value of $\eta \sim 0.4$ predicted in the average SFH case (Fig. 7, bottom panel). Note that the maximum thermally stable accretion rate is dependent on the η parameter and would be higher in the case of an impulsive burst of star formation.

However, simulations by Cuadra et al. (2006) find that the inflow rate for Sgr A* is reduced by up to an order of magnitude compared to the result in Quataert (2004) when the discreteness and disc geometry of stellar sources is taken into account, and recent results from Yusef-Zadeh et al. (2015) suggest that the inflow rate could be further reduced to $\dot{M}/\dot{M}_{\text{Edd}} \sim 3 \times 10^{-6}$ once clumping of stellar winds is taken into account.

6.2 Nuclear X-ray Luminosities

The unresolved core X-ray luminosities of nearby galactic nuclei provide a powerful diagnostic of the SMBH accretion rates and how they vary with SMBH mass and other galaxy properties (e.g., Ho 2008 and references therein). Figure 9 shows our predictions for $\langle L_X \rangle = \epsilon_X \dot{M} c^2$ as a function of black hole mass, where $\epsilon_X = \alpha \epsilon_{\text{rad}} \epsilon_{\text{bol}}$, $\alpha = 0.1$ accounts for the fraction of the inflowing matter loss to outflows from the accretion disc, ϵ_{rad} is the radiative efficiency of the accreted matter, and $\epsilon_{\text{bol}} = 0.1$ is the assumed bolometric correction into the measured X-ray band for low luminosity AGN (Ho 2008). In all cases the value of $\langle L_X \rangle$ is calculated using the accretion rate from the top line of equation (17) with $\Gamma = 0.7$ for $M_{\bullet} < 4 \times 10^7 M_{\odot}$, and $\Gamma = -0.3 \log_{10} \left(\frac{M_{\bullet}}{4 \times 10^7 M_{\odot}} \right) + 0.7$ for $M_{\bullet} \geq 4 \times 10^7 M_{\odot}$. This functional form is designed to approximately reproduce the behavior of $\Gamma(M_{\bullet})$ in the Lauer et al. (2007) sample.

The left panel of Figure 9 is calculated assuming a constant low value for the radiative efficiency of $\epsilon_X = 10^{-4}$, typical of those estimated for low luminosity AGN (e.g., Ho 2009). The right panel luminosities are calculated instead assuming an efficiency of $\epsilon_X = \epsilon_{\text{bol}} \epsilon_{\text{rad}}$ that depends on the Eddington ratio as predicted by MHD shearing box simulations by Sharma et al. (2007, see eq. [45] and surrounding discussion). Shown for comparison are the X-ray measurements (black stars) and upper limits (gray triangles) from the sample of early-type galaxies compiled by Miller et al. (2015, cf. Gallo et al. 2010). A black line shows the best power-law fit to the X-ray luminosity from Miller et al. (2015), given by $\langle L_X/L_{\text{Edd}} \rangle \sim M_{\bullet}^{\alpha}$ with $\alpha = -0.2$ (see also Zhang et al. 2009; Pellegrini 2010; Gallo et al. 2010). Also shown are the maximum accretion rates, respectively, for thermally stable accretion (eq. [29]; yellow), as set by SN Ia blow-out/heating (eq. [39]; teal), and as allowed by Compton heating feedback (eq. [46]; pink).

If the nuclei of elliptical galaxies are heated as expected for the average SFH of galaxies with similar mass, then to first order we predict that $\langle L_X/L_{\text{Edd}} \rangle$ should be an increas-

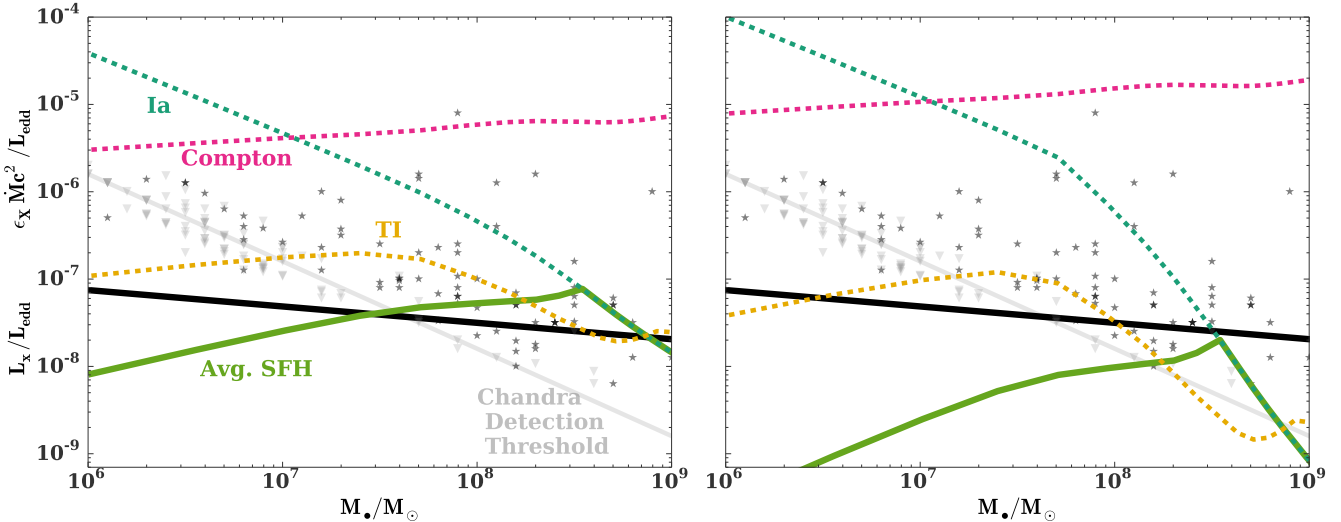


Figure 9. Average nuclear X-ray luminosity, $\langle L_X \rangle = \epsilon_X \dot{M} c^2$, as a function of SMBH mass. Green lines show our prediction in the case of heating due to the average SFH for galaxies corresponding to each black hole mass (Fig. 8), calculated using $\Gamma = 0.7$ for $M_\bullet < 4 \times 10^7 M_\odot$, and $\Gamma = -0.3 \log_{10}(M_\bullet / 4 \times 10^7 M_\odot) + 0.7$ for $M_\bullet \geq 4 \times 10^7 M_\odot$, as derived from the Lauer et al. (2007) sample. Shown for comparison are the measurements (black stars) and upper limits (gray triangles) for L_X/L_{edd} values, from the Miller et al. (2015) sample of early-type galaxies (a black line shows the best power-law fit $\langle L_X/L_{\text{edd}} \rangle \propto M_\bullet^\alpha$, with $\alpha = -0.2$). The left panel is calculated assuming a constant radiative efficiency $\epsilon_X = 10^{-4}(\epsilon_{\text{bol}}/0.1)$, while the right hand panel assumes $\epsilon_X = \alpha \epsilon_{\text{bol}} \epsilon_{\text{rad}}$, where ϵ_{rad} is the radiative efficiency of low luminosity accretion discs calculated by Sharma et al. (2007) (eq. [45]) and $\alpha = 0.1$ is the fraction of the mass inflowing on large scales that reaches the SMBH. Shown for comparison are the X-ray luminosities calculated for the maximum thermally-stable accretion rate (dashed orange line; eq. [29]); the SN Ia-regulated accretion rate (dashed teal line; eq. [39]), and the Compton heating-regulated accretion rate (dashed pink line; eq. [44])¹⁰, again all calculated for the average SFH corresponding to each SMBH mass.

ing function of BH mass. This result is in tension with the observed down-sizing trend: the average Eddington ratio is seen to decrease (albeit weakly) with M_\bullet , especially in the model where ϵ_X increases with the Eddington ratio. However, one must keep in mind the enormous uncertainty in calculating the luminosity of the accretion flow close to the black hole in a single waveband based on the feeding rate on larger scales. Also, if disc outflows indeed carry away most of the infalling mass before it reaches X-ray producing radii (e.g. Blandford & Begelman 1999; Li et al. 2013), then the angular momentum of the infalling gas might also influence the X-ray luminosity indirectly through the inflow efficiency α , in a way that could depend systematically on the stellar population and hence M_\bullet . However, in general the efficiency with which inflowing matter reaches the SMBH (and hence X-ray luminosity) would naively be expected to decrease with decreasing M_\bullet due to the increasing angular momentum of low mass galaxies, exacerbating the tension between our findings and the observed downsizing trend.

Perhaps a more readily addressable test is whether a steady-state accretion picture developed in this work can account for the the large scatter, typically of 2 – 3 orders of magnitude, in L_X/L_{edd} at fixed M_\bullet . Scatter could result from the strong sensitivity of the accretion rate to the stellar wind velocity and mass loss parameter, $\dot{M}/\dot{M}_{\text{edd}} \propto v_w^{-3.8(-2.4)}$ for core(cusp) galaxies, respectively (Fig. 4; eq. [18]). When combined with the significant dependence of v_w on stochastic intermittency in the star formation history (Appendix B2), this can lead to order of magnitude differences in \dot{M} . However, we note that v_w is not expected

to vary by more than a factor of a few for a thermally-stable flow, limiting the allowed variation of $\dot{M}/\dot{M}_{\text{edd}}$. The discrete nature of stellar wind sources and their motions could result in an additional order of magnitude variation \dot{M} (Cuadra et al. 2008).

Variations in L_X/L_{edd} could also result from differences in angular momentum of the infalling gas from galaxy to galaxy, resulting in differences in the fraction of the gas lost to outflows. Also potentially contributing is the order of magnitude difference, at fixed v_w and M_\bullet , between \dot{M} for core and cusp galaxies (Fig. 8). Differences in \dot{M} are augmented by the theoretical expectation that $L_X \propto \dot{M}^2$ for radiatively inefficient flows.

6.3 Steady Accretion versus outbursts

It is also possible, and indeed likely, that many of the Miller et al. (2015) sample of galactic nuclei are not accreting in steady state. This is supported by the fact that many of the X-ray luminosities in Figure 9 lie above the predictions for stable accretion, i.e., $L_X \gtrsim \epsilon_X \dot{M}_{\text{TI}} c^2$ (yellow line), at least for our choice of radiative efficiency.

Within our steady state solutions, gas outside the stagnation radius r_s is blown out in wind. However, for very massive galaxies ($M_\bullet \gtrsim 10^8 M_\odot$), the energy injected into the gas is not enough to truly eject it from the potential well of the galaxy, even if the gas is blown out of the stellar bulge (e.g. even if the $\zeta > \zeta_c$ criterion is satisfied—see equation (16) and surrounding discussion). This gas is likely to build up on the outskirts of the galaxy until a thermal in-

stability develops, causing the CNM to undergo cyclic oscillations of rapid cooling and high accretion rates, followed by quiescent periods once gas has been consumed and/or AGN feedback becomes effective. Such cycles are seen in numerical simulations of elliptical galaxies on large scales and long time-scales (Ciotti et al. 2010). Evidence for such periodic outbursts includes observations showing that a fraction of early-type galaxies in the local Universe have undergone recent ($< 1 - 2$ Gyr old) star formation episodes (Donas et al. 2007).

If the actual radiative efficiency is lower than our fiducial assumption, then an even larger fraction of the X-ray detections would lie above the predictions for stable accretion. For example, we assume that a fraction $\alpha = 0.1$ of the mass inflow rate reaches the SMBH, but this fraction could be considerably smaller. In such a case the X-ray detected galaxies will experience less heating than we calculate for the average SFH, and may not be stably accreting at all. This is plausible given that the Miller et al. (2015) sample includes only early-type galaxies with older stellar populations than the average for their stellar mass.

Figure 8 (top panel) also shows that $\dot{M}_C > \dot{M}_{\text{TI}}$ across all black hole masses. This indicates that Compton heating is not sufficient to produce a thermally stable accretion rate, at least for conditions corresponding to the average SFH.

Similar cyclic AGN activity could occur on the smaller radial scale of the sphere of influence (e.g. Yuan & Li 2011, Cuadra et al. 2015). In this case the large scatter in the X-ray luminosities shown in Fig 9 could result from the wide range of inflow rates experienced over the course of a cyclic episode between instabilities and periodic nuclear outbursts.

If the galaxies with measured L_X at low M_\bullet in Figure 9 are indeed in a state of thermally-unstable outburst, then some of the galaxies with X-ray upper limits could be contributing to a separate population of thermally-stable, steadily accreting nuclei. Such a population could include SgrA*, which has a much lower X-ray luminosity for its SMBH mass than predicted by the Miller et al. (2015) trend. A potentially bimodal population of steady and outbursting galactic nuclei calls into question the practice of using simple extrapolations of power-law fits to the $L_X(M_\bullet)$ relationship to low M_\bullet to constrain the occupation fraction of SMBHs in the nuclei of low mass galaxies.

6.4 SMBH Growth Times

Low-mass AGN in the local Universe with $M_\bullet \lesssim 3 \times 10^7 M_\odot$ are observed to be growing on a time-scale comparable to the age of the Universe, while the most massive SMBHs with $M_\bullet \gtrsim 10^9 M_\odot$ possess local growth times which are more than 2 orders of magnitude longer (Heckman et al. 2004; Kauffmann & Heckman 2009).

The bottom panel of Figure 8 shows the SMBH growth time, $t_{\text{grow}} \equiv M_\bullet / \dot{M}_\bullet$, for each accretion rate shown in the top panel, recalling that $\dot{M}_\bullet = \alpha \dot{M}$, where $\alpha = 0.1$. For SMBHs which accrete steadily at the rate set by stellar wind heating due to the average star formation history of their host galaxies, we see that t_{grow} exceeds the Hubble time by 2–4 orders of magnitude across all M_\bullet . Steady accretion therefore cannot explain the growth of low mass black holes, a fact which is not surprising given that approximately half of this growth occurs in AGN radiating within 10 per cent

of their Eddington rate (Heckman et al. 2004). Such high accretion rates likely instead require a source of gas external to the nuclear region, triggered either by galaxy mergers associated with the hierarchical growth of structure or thermal instabilities on larger, galactic scales (e.g. Ciotti et al. 2010, Voit et al. 2015).

That the growth time associated with thermally-unstable accretion (yellow line in Fig. 8) exceeds the Hubble time across all SMBH masses highlights the fact that significant black hole growth in the local Universe cannot result from thermally-stable steady accretion of gas lost from the surrounding stellar population studied in this paper. Gas blow-out by SN Ia cannot alone prevent the growth of low-mass black holes, as indicated by the low growth times $\ll t_h$ allowed by Ia heating (green lines), although Ia heating could play in principle a role in capping the growth rate of $\gtrsim 10^8 M_\odot$ black holes, again depending on the efficiency of Ia heating.

6.5 TDE Jets

Our results also have implications for the environments encountered by relativistic jets from TDEs. For low-mass SMBHs with $M_\bullet \lesssim 10^7 M_\odot$, such as that responsible for powering the transient *Swift* J1644+57 (Bloom et al. 2011), we predict gas densities of a $n \sim \text{few cm}^{-3}$ on radial scales of 0.3 pc for wind heating rates within the physically expected parameters $v_w \sim 500 - 1000 \text{ km s}^{-1}$ and $\eta = 0.4$ (see Fig. 2). This is comparable to the density $\sim 0.3 - 10 \text{ cm}^{-3}$ obtained by modeling the radio afterglow of *Swift* J1644+57 (Berger et al. 2012, Metzger et al. 2012). However, there is considerable uncertainty in the afterglow modeling. For example, Mimica et al. (2015) find a much higher density of 60 cm^{-3} at 0.3 pc.

Berger et al. (2012) infer a flattening of the gas density profile of the host of J1644+57 on radial scales $r \gtrsim 0.4 \text{ pc}$ (their Fig. 6) which looks qualitatively similar to the shape of the density profile we predict for core galaxies (Fig. 2, solid line). To obtain such a flattening on the inferred radial scales would require a black hole of $M_\bullet \sim 10^7 M_\odot$. However, this is inconsistent with the break in the gas density seen at $\sim 0.6 \text{ pc}$ by Berger et al. (2012), which should correspond to the break radius of the *stellar density* profile, thus implying an unrealistically small SMBH mass of $M_\bullet \simeq 100 M_\odot$ according to the mean $r_b - M_\bullet$ relationship (Lauer et al. 2007). Alternatively, the observed density break in J1644+57 could result from the outer edge of a sub-parsec nuclear star cluster (e.g., Carson et al. 2015). The high stellar densities of such a compact star cluster could greatly enhance the TDE rate (e.g. Stone & Metzger 2014), possibly making this association uncoincidental. On the other hand, we note that some models for J1644+57 (e.g., Tchekhovskoy et al. 2014) favor a much smaller black hole ($10^5 - 10^6 M_\odot$) than we estimate would be required to produce the observed inner break.

6.6 Regulation by SMBH Kinetic Feedback

Our analysis of SMBH feedback has focused on Compton heating instead of kinetic feedback, since the effects of radiative feedback are relatively straightforward to calculate from the properties of the accretion flow. However, it is possible kinetic feedback from SMBH outflows could play an equal or greater role in regulating accretion, even in low luminosity AGN.

Our simple parameterization of kinetic feedback (eq. [48]) assumes a uniform volumetric heating and predicts an effective wind velocity which increases with SMBH mass as $v_w \propto M_\bullet^{0.38}$ for core and cusp galaxies, respectively. Coupled with the dependence of the SMBH accretion rate on the wind heating, $\dot{M}/\dot{M}_{\text{edd}} \propto M_\bullet^{0.76(0.48)} v_w^{-3.8(-2.4)}$ (Fig. 4; eq. [18]), a dominant source of kinetic feedback of the form we have adopted leads to an Eddington ratio dependence on SMBH mass of $\dot{M}/\dot{M}_{\text{edd}} \propto M_\bullet^{-0.7(-0.4)}$.

This prediction is more in line with the observed dependence of $\langle L_X/L_{\text{edd}} \rangle$ in elliptical galaxies (Fig. 9, green line), suggesting that accretion regulation by kinetic feedback could play a role in determining the X-ray luminosities of elliptical galaxies. However, our assumption that kinetic outflows heat the gas uniformly in volume is rather arbitrary and would need to be more rigorously justified by numerical studies of how jets or disc outflows couple energy to their gaseous environment. As already discussed, it is furthermore unclear whether a steady-state accretion model is at all relevant in the case when SMBH feedback dominates due to the time delay between the small scale accretion flow and the thermodynamic response of the CNM on larger scales.

7 CONCLUSIONS

We have calculated steady-state models for the hot gaseous circumnuclear media of quiescent galaxies, under the assumption that gas is supplied exclusively by stellar wind mass loss and heated by shocked stellar winds, supernovae and black hole feedback. We numerically compute solutions for a range of different black hole masses, heating rates, and observationally-motivated stellar density profiles. Then we use our numerical results (Table 2) to verify and calibrate analytic relationships (Appendix A). We use the latter to explore systematically how the SMBH accretion rate varies with black hole mass and the galaxy’s SFH. Our results for $\dot{M}(M_\bullet)$ are compared with observed trends of the nuclear X-ray luminosities of quiescent SMBHs and low luminosity AGN. Our conclusions are summarized as follows.

(i) A stagnation radius, r_s , divides the nuclear gas between an accretion flow and an outgoing wind. In steady-state the gas inflow rate towards the black hole is proportional to the stellar mass enclosed inside of r_s . In the limit of strong heating, the stagnation radius resides interior to the SMBH influence radius and coincides with the Bondi radius (eq. [22]). In the limit of weak heating ($\zeta < \zeta_c$; eq. [16]), the stagnation radius moves to large radii, near or exceeding the

stellar break radius $r_b \gg r_{\text{inf}}$, greatly increasing the density of gas on smaller radial scales.

(ii) In the vicinity of the stagnation radius, including the effects of heat transport by electron conduction results in at most order unity changes to the key properties of the flow (e.g. stagnation radius, mass accretion rate, and thermal stability) for causal values of the conduction saturation parameter $\phi < 0.1$ (eq. [23]). However, in principle heat conduction of heat from the inner accretion flow can affect the solution properties on much larger scales (Johnson & Quataert 2007). For example, Tanaka & Menou (2006) find that conductivity can contribute to driving bipolar outflows.

Angular momentum of the gas will become important on small scales, where gas stopped by a centrifugal barrier and unable to cool could drive outflows near the equatorial and polar regions of the flow.

(iii) Radiative cooling has a more pronounced influence on the flow structure when the radiative cooling rate exceeds the gas heating rate near the stagnation radius, where the gas is in nearly hydrostatic equilibrium (Fig. 1). This condition is approximately equivalent to the $t_{\text{cool}} \lesssim 10t_{\text{ff}}$ criterion for thermal instability advocated by e.g. Sharma et al. (2012), Gaspari et al. (2012b) and Li & Bryan (2014a). The transition in the flow properties that occurs as heating is reduced may represent a true “thermal instability” (hot ISM condensing into a cooler clouds), or it may simply represent an abrupt transition from a steady inflow-outflow solution to a global cooling flow. We leave distinguishing between these possibilities to future work.

(iv) The location of the stagnation radius, and hence the inflow rate, is a sensitive function of the gas heating rate $\propto v_w^2$. Quantitatively, $r_s \propto v_w^{-2}$, implying that $\dot{M} \propto v_w^{-3.8(-2.4)}$ for fiducial core (cusp) galaxies. However, \dot{M} can increase even more rapidly with decreasing v_w for two reasons: (1) when v_w becomes comparable to the stellar velocity dispersion ($\zeta < \zeta_c$; eq. [16]), then gas remains bound to the stellar bulge and cannot produce an outflow interior to the stellar break radius (2) For low v_w , gas near the stagnation radius becomes thermally unstable, which based on the results of previous numerical studies (e.g. Ciotti et al. 2010) is instead likely to result in a burst of high accretion (§6.3).

(v) Stellar wind heating, supernovae, and AGN feedback depend explicitly on the SMBH mass as well as the SFH in the galactic nucleus. A young starburst of age $\lesssim 10$ Myr produces mass and energy injection dominated by young stellar winds ($v_w \sim 1000 \text{ km s}^{-1}$) and supernovae, while for exclusively old stellar populations mass input is dominated by AGB winds and heating is dominated by AGN feedback and supernovae. Ongoing, continuous star formation presents a hybrid situation, with energy input usually dominated by young stars and mass input dominated by old stars (Appendix B). Galactic nuclei with $M_\bullet \lesssim 10^8 M_\odot$ that are heated according to their average SFHs (as derived from cosmological simulations) receive a stellar wind heating of $v_w \sim 700 \text{ km s}^{-1}$. This heating can be suppressed if the star formation is sufficiently intermittent (Fig. B2).

(vi) Type Ia SNe only provide a continuous heating source exterior to the Ia radius r_{Ia} (eq. [36]) where the time between subsequent SNe exceeds the dynamical time-scale. Non-Ia heating due to the average SFH results in $r_s < r_{\text{Ia}}$, except for the most massive galaxies (Fig. 7). However, if r_s does

¹⁰ These equation correspond to the specific cases of $\Gamma = 0.1$ and $\Gamma = 0.8$, but it is straightforward to generalize these for arbitrary Γ as we do for this figure.

approach r_{Ia} , then SN Ia heating is usually large enough to prevent r_s from greatly exceeding r_{Ia} . SNe Ia thus regulate the SMBH accretion rate below the value \dot{M}_{Ia} (eq. [39]), except possibly in high mass elliptical galaxies with large break radii and $\zeta(v_w^{\text{Ia}}) \gtrsim \zeta_c$.

(vii) Unlike stellar heating, heating from SMBH feedback depends on the accretion rate, which itself depends on the heating. Compton heating is generally unimportant compared to stellar wind heating for the average SFH, but it can be significant in the case of an impulsive starburst (Fig. 6). However, SMBH feedback may not be capable of truly stabilizing the flow given its inability to respond instantaneously to local changes in the properties of the gas. Kinetic feedback could also be important in determining $\dot{M}(M_\bullet)$ when stellar heating is weak (§6.6) but is more challenging to quantify.

(viii) Stellar wind heating from the average SFH may be sufficient to permit thermally-stable, steady-state accretion, depending on the accretion efficiency of the SMBH. However, the resulting average Eddington-normalized accretion rate is predicted to increase with M_\bullet (Fig. 9), in tension with the (also weak) downsizing trend of measured X-ray luminosities in early-type galactic nuclei (e.g., Miller et al. 2015). Thermally stable accretion models can reproduce the observed scatter in nuclear X-ray luminosities at fixed M_\bullet (two to four orders of magnitude) due to the combination of (1) differences in the stellar wind heating rate due to stochastic variation in SFH between galaxies, or within one galaxy due to burstiness in the SFH, as in Fig. B2; (2) variations in the amount of inflowing mass which is lost to small scale outflows from the SMBH accretion disc, likely due to variations in the angular momentum of the accreting gas (cf. Pellegrini 2010).

(ix) However, for lower X-ray radiative efficiencies, the accretion rates of early-type galaxies are above the maximum value for thermally stable flow, \dot{M}_{TI} (Fig. 9). This implies that current X-ray detections could instead be comprised mostly of nuclei undergoing outburst due to thermal instabilities. In such a case, there may exist a separate (usually undetected) branch of low- L_X nuclei accreting stably. The existence of such a bimodal population would call into question constraints on the SMBH occupation fraction in low mass galaxies (Miller et al. 2015) derived by extrapolating the $L_X(M_\bullet)$ relationship to small M_\bullet .

(x) Low mass black holes grow in the low redshift Universe over time-scales comparable to the Hubble time (Heckman et al. 2004). The accretion rates so required are too high to be consistent with either the value predicted for the average SFH history or the maximum allowed for steady-state, thermally stable accretion (Fig. 8). Perhaps unsurprisingly, low- M_\bullet growth and AGN activity must instead be driven by a supply of gas external to the nucleus, such as galaxy mergers or thermal instabilities on larger, galactic scales (e.g. Voit et al. 2015).

We conclude by drawing attention to a few limitations of our model. First, we have neglected any large scale inflow of gas to the nucleus by assuming the only source of gas feeding the black hole is stellar wind mass loss from the local stellar population. Our estimates represent a lower bound on the time averaged gas density of the CNM. Although our model can, under certain assumptions, describe quiescent galactic nuclei, it cannot account for AGN.

Predictions for the SMBH accretion rate are strongly tied to the age and radial distribution of the stellar population within the sphere of influence. Our model therefore cannot make definitive predictions for the accretion mode of individual galaxies without knowledge of their specific SFH. We adopt halo-averaged star formation rates measured using multi-epoch abundance matching models by Moster et al. (2013), and neglect any spatial variation in the star formation rate for any given galaxy. However, galaxies of mass $\gtrsim 7 \times 10^{10} M_\odot$ assemble their stars from the inside out (Perez et al. 2013), resulting in galactic nuclei which may be systematically older than assumed in our model and thus more prone to thermal instability.

Finally, we do not account for the effects of non-spherical geometry or discreteness of stellar wind sources (Cuadra et al. 2006, 2008). We assume all of the mass and energy sources are efficiently mixed, and do not take into account the possibility of slower wind material condensing into high density structures (as described in Cuadra et al. 2005) or some of the energy injection leaking away in 3-D (Harper-Clark & Murray 2009; Zubovas & Nayakshin 2014).

ACKNOWLEDGMENTS

We thank the referee, Sergei Nayakshin, for several insightful comments. We acknowledge helpful conversations with Greg Bryan, Jenny Greene, Jules Halpern, Kathryn Johnston, Jerry Ostriker, Eliot Quataert, Massimo Gaspari and Takamitsu Tanaka. This work relied on Columbia University’s Yeti computer cluster, and we acknowledge the Columbia HPC support staff for assistance. BDM gratefully acknowledges support from NASA *Fermi* grant NNX14AQ68G, NSF grant AST-1410950, and the Alfred P. Sloan Foundation.

APPENDIX A: DERIVATION OF STAGNATION RADIUS

Here we derive an analytic expression for the time-independent stagnation radius, r_s . In steady-state, the requirement that the net heating rate on the right hand side of the entropy equation (eq. [7]) must equal zero at the stagnation radius (where $v = 0$) fixes the temperature at r_s :

$$\frac{\gamma}{\gamma-1} \frac{p}{\rho} \Big|_{r_s} = \frac{\tilde{v}_w^2|_{r_s}}{2} \Rightarrow \frac{k_b T|_{r_s}}{\mu m_p} = \frac{\gamma-1}{\gamma} \frac{\tilde{v}_w^2|_{r_s}}{2} \quad (\text{A1})$$

Combining (eq. [7]) with the first law of thermodynamics,

$$T \frac{ds}{dr} \Big|_{r_s} = \frac{1}{\gamma-1} \frac{d(p/\rho)}{dr} \Big|_{r_s} + \frac{\nu}{r_s} \frac{p}{\rho} \Big|_{r_s} = \underbrace{\frac{q(\frac{v^2}{2} + \frac{\tilde{v}_w^2}{2} - \frac{\gamma}{\gamma-1} \frac{p}{\rho})}{\rho v}}_A \Big|_{r_s}, \quad (\text{A2})$$

where $\nu \equiv -d \ln \rho / d \ln r|_{r_s}$. The right side can be evaluated using L'Hopital's rule, yielding

$$\lim_{r \rightarrow r_s} A = \frac{d}{dr} \left[\left(\frac{v^2}{2} - \frac{\gamma}{\gamma-1} \frac{p}{\rho} + \frac{\tilde{v}_w^2}{2} \right) \right]_{r_s} \approx -\frac{\gamma}{\gamma-1} \frac{d(p/\rho)}{dr} \Big|_{r_s} - \frac{3}{2(2+\Gamma)} \frac{GM_\bullet}{r_s^2}, \quad (\text{A3})$$

where we have used the definition $\tilde{v}_w^2 = v_w^2 + \frac{3}{2+\Gamma} \frac{GM_\bullet}{r}$ + σ_0^2 (eq. [9]). Substituting this expression back into equation (A2) and using equation (A1) gives

$$\frac{\gamma+1}{\gamma-1} \frac{d(p/\rho)}{dr} \Big|_{r_s} + \frac{\gamma-1}{\gamma} \frac{\nu}{r_s} \frac{\tilde{v}_w^2|_{r_s}}{2} = -\frac{GM_\bullet|_{r_s}}{2r_s^2} - \frac{3}{2+\Gamma} \frac{GM_\bullet}{2r_s^2}. \quad (\text{A4})$$

Combining this with condition of hydrostatic equilibrium (eq. [6]) at the stagnation point,

$$\frac{1}{\rho} \frac{dp}{dr} \Big|_{r_s} = -\frac{GM_{\text{enc}}}{r_s^2} \Rightarrow \frac{d(p/\rho)}{dr} \Big|_{r_s} + \frac{p}{\rho} \underbrace{\frac{d \ln(\rho)}{dr}}_{-\nu/r} = -\frac{GM_{\text{enc}}}{r_s^2}, \quad (\text{A5})$$

results in the following expression for the stagnation radius:

$$r_s = \frac{GM_\bullet}{\nu \tilde{v}_w^2|_{r_s}} \left(4 \frac{M_\star|_{r_s}}{M_\bullet} + \frac{13+8\Gamma}{4+2\Gamma} \right) = \frac{GM_\bullet}{\nu(v_w^2 + \sigma_0^2)} \left[4 \frac{M_\star|_{r_s}}{M_\bullet} + \frac{13+8\Gamma}{4+2\Gamma} - \frac{3\nu}{2+\Gamma} \right] \quad (\text{A6})$$

where we have assumed $\gamma = 5/3$. This relationship can be reparameterized as

$$\frac{r_s}{r_{\text{inf}}} = \frac{1}{3\nu\zeta^2} \left[4 \frac{M_\star|_{r_s}}{M_\bullet} + \frac{13+8\Gamma}{4+2\Gamma} - \frac{3\nu}{2+\Gamma} \right], \quad (\text{A7})$$

where $r_{\text{inf}} \equiv 3GM_\bullet/\sigma_0^2$ and we have defined $\zeta \equiv \sqrt{1 + (v_w/\sigma_0)^2}$. Because $M_\star|_{r_s} = M_\bullet(r_s/r_{\text{inf}})^{2-\Gamma}$, in general equation (A7) must be solved implicitly for r_s/r_{inf} . However, when $M_\star|_{r_s} \ll M_\bullet$ or equivalently $r_s \ll r_{\text{inf}}$, equation (A7) simplifies considerably:

$$r_s = \frac{13+8\Gamma}{4+2\Gamma} \frac{GM_\bullet}{\nu \tilde{v}_w^2} \quad (\text{A8})$$

APPENDIX B: ANALYTIC MODEL FOR DEPENDENCE OF WIND HEATING v_w^* ON STELLAR AGE

B1 Single Burst

In the case of a single impulsive burst of star formation, the mass and energy injection rate per unit stellar mass at time t after the burst are given, respectively, by

$$\dot{m}(t) = f_{\text{TO}} \dot{m}_{\text{TO}} + f_{\text{OB}} \dot{m}_{\text{OB}} \quad (\text{B1})$$

$$\dot{e}(t) = f_{\text{OB}} \dot{e}_{\text{OB}}(t) + f_{\text{MS}} \int_{m_0}^{m_{\text{T}}(t)} \frac{\tilde{v}_w^2(M_\star, t) \dot{m}(M_\star, t) \mu|_{M_\star} dM_\star}{\bar{m}_\star}, \quad (\text{B2})$$

where the f 's represent the efficiency with which each source of mass/energy injection is thermalized (we take all of the f 's to be 1). In the top line, the first term corresponds to mass injection due winds from post-main sequence stars. The second term corresponds to mass injection due to stellar winds from massive stars. For the latter we use population synthesis calculations by Voss et al. (2009). From the bottom panel of their Figure 7, the stellar wind mass loss rate per massive star can be approximated to within a factor of a few by

$$\dot{M} = \begin{cases} 10^{-6.5} M_\odot \text{yr}^{-1} & t < 4 \text{ Myr} \\ 10^{-5.4} M_\odot \text{yr}^{-1} \left(\frac{t}{4 \times 10^6 \text{ yr}} \right)^{-3} & 4 \text{ Myr} \leq t \leq 40 \text{ Myr.} \\ 0 & t > 40 \text{ Myr.} \end{cases} \quad (\text{B3})$$

$\dot{m}_{\text{OB}} = f_8 \dot{M}/\bar{m}_\star$, where $f_8 = 2.6 \times 10^{-3}$ is the fraction of the stellar mass with $M_\star > 8M_\odot$ and $\bar{m}_\star = 0.35 M_\odot$ is the mean stellar mass for our assumed Salpeter IMF, $\mu \sim M_\star^{-2.35}$.

For the mass loss rate from post-main sequence winds, we take

$$\dot{m}_{\text{TO}} = \frac{\Delta M(t) \dot{M}_{\text{TO}}(t) \mu|_{M_{\text{TO}}(t)}}{\bar{m}_\star} \quad t \geq 40 \text{ Myr}, \quad (\text{B4})$$

and 0 for earlier times. By truncating \dot{m}_{TO} at 40 Myr, we are ignoring the non-steady mass injection by type II supernovae.

The quantity of mass lost in post-main sequence winds $\Delta M(t)$ is estimated from the expression given by Ciotti & Ostriker (2007) (their eq. [10]),

$$\Delta M = \begin{cases} 0.945 M_{\text{TO}} - 0.503 & M_{\text{TO}} < 9 M_\odot \\ M_{\text{TO}} - 1.4 M_\odot & M_{\text{TO}} \geq 9 M_\odot, \end{cases} \quad (\text{B5})$$

where M_{TO} is the turn-off mass, which at time $t < t_h$ is calculated as

$$\log(M_{\text{TO}})/M_\odot = 0.24 + 0.068x^2 - 0.34x + 4.76e^{-4.58x}, \quad (\text{B6})$$

where $x = \log(t/10^9 \text{ yr})$. This functional fit is designed to reproduce the results of Maeder & Meynet (1987) (their Table 9) for massive stars while asymptoting to the formula provided by Ciotti & Ostriker (2007) (their eq. [9]) for intermediate and late times ($t \gtrsim 10^8$ years).

The first term in equation (B2) corresponds energy injection from massive stars, while the second term accounts

for energy injection from stars on the lower main sequence. Both terms have a thermalization efficiency, f , which we take to be 1. Note we do not account for energy from Type II supernovae.

The MS wind mass loss rate $\dot{m}(M_*, t)$ is calculated based on the generalization of Reimer's law

$$\dot{m} = 4 \times 10^{-13} \frac{L_* R_*}{M_*} M_\odot \text{yr}^{-1}, \quad (\text{B7})$$

where R_* , L_* , T_{eff} and g_* are the stellar radius, luminosity, effective temperature, and surface gravity, respectively, the latter normalized to its solar value g_\odot . The stellar radius and luminosity are estimated as (Kippenhahn & Weigert (1990); Figs. 22.2) 22.3)

$$L_* = \begin{cases} L_\odot (M_*/M_\odot)^{3.2} & M_* > M_\odot \\ L_\odot (M_*/M_\odot)^{2.5} & M_* \leq M_\odot \end{cases} \quad (\text{B8})$$

$$R_* = \begin{cases} R_\odot (M_*/M_\odot)^{0.57} & M_* > M_\odot \\ R_\odot (M_*/M_\odot)^{0.8} & M_* \leq M_\odot \end{cases} \quad (\text{B9})$$

The wind velocity of main sequence winds is assumed to equal $v_w(M_*, t) = v_{w,\odot} (M_*/M_\odot)^{1/2} (R_*/R_\odot)^{-1/2}$, i.e. scaling as the stellar escape velocity and normalized to the velocity of the solar wind $v_{w,\odot} = 430 \text{ km s}^{-1}$; this produces an effective wind heating velocity for main sequence winds alone of $\sim 100 \text{ km s}^{-1}$ for $\tau_* \sim t_h$, close to the value found by Naiman et al. (2013) for globular clusters based on a more sophisticated population synthesis treatment.

Winds from lower main sequence stars only dominate the energy injection a late times $\sim 10 \text{ Gyr}$ after an impulsive burst of star formation. Even with 100% thermalization efficiency these winds could not thermally stabilize the CNM.

The rate of energy injection due to winds from massive stars, $\dot{e}_{\text{OB}}(t) = f_8 \dot{\mathcal{E}}/\dot{m}_*$, where $f_8 = 2.6 \times 10^{-3}$ is the fraction of the stellar mass with $M_* > 8M_\odot$ for our assumed Salpeter IMF. Here $\dot{\mathcal{E}}(t)$ is the energy injection rate per massive star, which we estimate as

$$\dot{\mathcal{E}}(t) = 1.3 \times 10^{36} \text{ erg s}^{-1} \begin{cases} 1 & t < 4 \times 10^6 \text{ yr} \\ \left(\frac{t}{4 \times 10^6 \text{ yr}}\right)^{-3.73} & 4 \times 10^6 \text{ yr} \leq t \leq 10^8 \text{ yr} \\ 0 & t > 10^8 \text{ yr} \end{cases} \quad (\text{B10})$$

based on the results of Voss et al. (2009) (their Fig. 7, top panel), who use a population synthesis code to simulate the mass and energy injection into the ISM from an OB association. Although equation is valid only for $t \lesssim 10 \text{ Myr}$, in practice the precise functional form of $\dot{e}_{\text{OB}}(t)$ is generally unimportant for our purposes, so we adopt equation as being valid for all times.

The effective wind velocity in the limit of an impulsive star formation may then be written as

$$\bar{v}_w(t) = 2\dot{e}(t)/\dot{m}(t) \quad (\text{B11})$$

while

$$\eta = \dot{m}(t)t_h \quad (\text{B12})$$

Figure B1 shows the values of $\bar{v}_w(t)$ and $\eta(t)$ as a function of stellar age, τ_* .

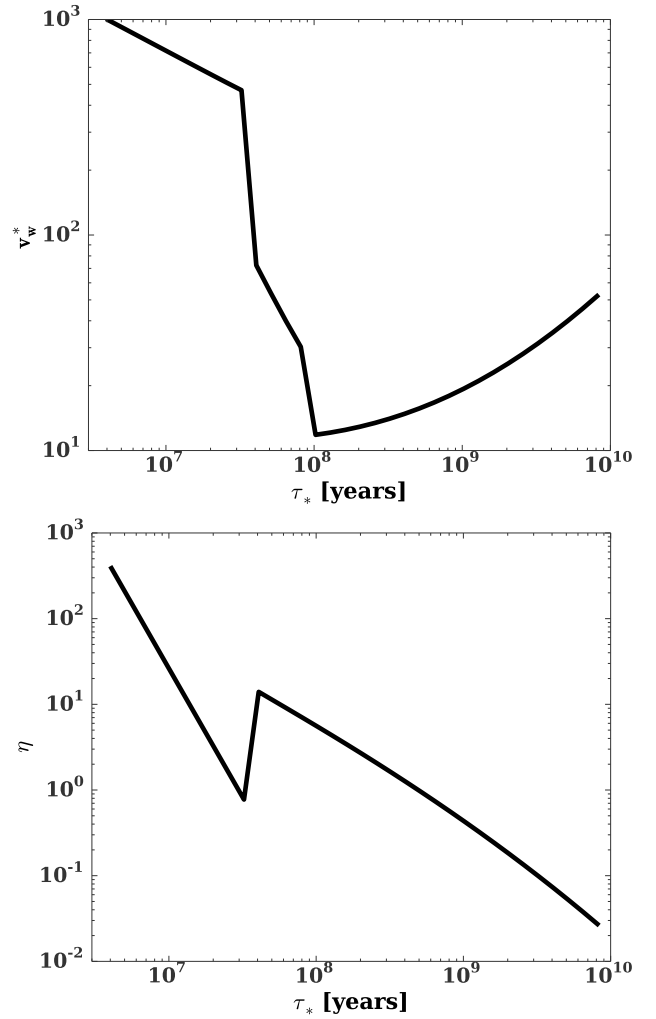


Figure B1. Effective heating rate, v_w^* , and mass loss parameter, η (eq. [8]), resulting from stellar winds from a stellar population of age τ_* .

B2 Over Star Formation History

Generalizing to an arbitrary SFH $S(t)$, the total rate of mass and energy input can be written as

$$\dot{M}(t) = \int_0^t S(t_1) \dot{m}(t - t_1) dt_1 \quad (\text{B13})$$

$$\dot{E}(t) = \int_0^t S(t_1) \dot{e}(t - t_1) dt_1, \quad (\text{B14})$$

resulting in a wind heating parameter of

$$v_w^2(t) = 2\dot{E}(t)/\dot{M}(t). \quad (\text{B15})$$

The mass return parameter will be

$$\eta = \frac{\dot{M}(t)}{\int_0^t S(t_1) dt_1} t_h \quad (\text{B16})$$

We estimate the stellar wind heating provided by the *average* star formation history of galaxies of a given M_\bullet using the results of Moster et al. (2013, eqs. 17-20). Note that the star formation histories in Moster et al. (2013) are in terms of halo mass. For a given M_\bullet we assign the halo mass

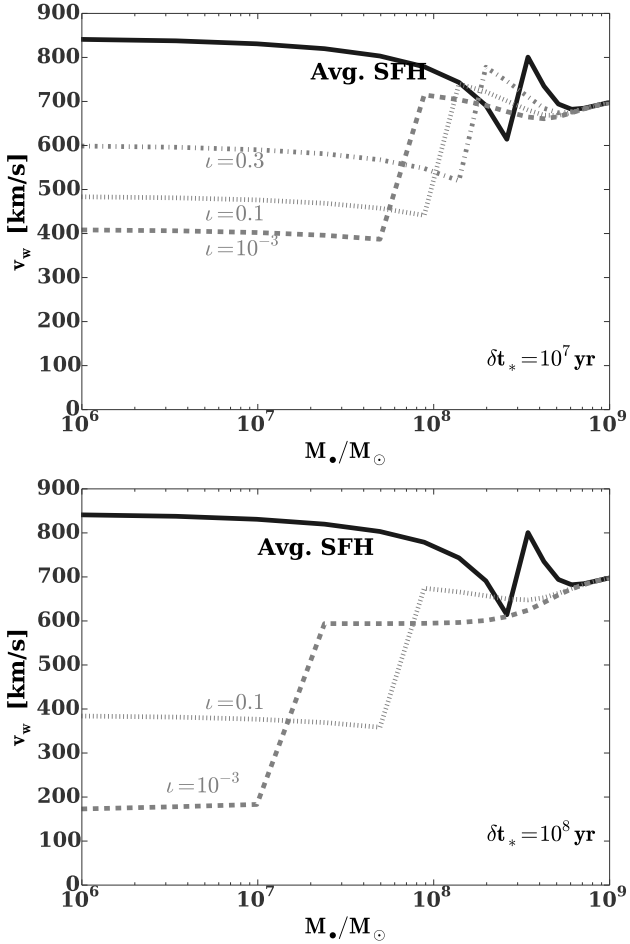


Figure B2. Effective wind velocities for nonstandard star formation histories. The black curves shows, for reference, v_w calculated using the halo-averaged $S(t)$, and gray curves show wind heating resulting from perturbed star formation histories given by equation (B24). In the top panel the star formation rate declines for a time, δt_* = 10^7 years to fractions $\iota = 0.001$ (dashed), $\iota = 0.1$ (dotted), and $\iota = 0.3$ (dot-dashed) of the halo averaged value. The bottom panel shows results for $\delta t_* = 10^8$ years and $\iota = 0.001$ (dashed) and 0.1 (dotted).

whose star formation history would produce a bulge consistent with the $M_\bullet - M_{\text{bulge}}$ relationship from [McConnell & Ma \(2013\)](#). A slight complication occurs for the largest mass halos, where much of the $z = 0$ stellar mass has been acquired through accretion of satellite halos rather than *in situ* star formation. To accommodate this, we incorporate analytic fits for mass accretion histories, taken from [Moster et al. \(2013\)](#), their eqs. 21-23), assuming that the age distribution of the accreted stars is equal to the age distribution of those formed *in situ*. This assumption may be conservative if the primary galaxy’s accretion history is dominated by minor mergers with younger stellar populations. On the other hand, the dynamical friction inspiral time for small satellite galaxies is quite long, generally much greater than the $\sim 10^7$ yr for which young stars can dominate the heating budget. The mass of stars accreted for halo masses, $M_{\text{halo}} < 3 \times 10^{12} M_\odot$, and redshifts, $z > 4$, is small and is neglected.

To find the total mass ($\dot{M}'(t)$) and energy ($\dot{E}'(t)$) injection rates, including the contribution of accreted stars, we add a convolution of the specific mass and injection rates with the accretion history $A(t)$ to the mass and energy injection rates from star formed *in-situ*. Thus,

$$\dot{M}'(t) = \dot{M}(t) + \int_0^t A(t_{\text{acc}}) \frac{\dot{M}(t_{\text{acc}})}{\int_0^{t_{\text{acc}}} S(t_1) dt_1} dt_{\text{acc}} \quad (\text{B17})$$

$$\dot{E}'(t) = \dot{E}(t) + \int_0^t A(t_{\text{acc}}) \frac{\dot{E}(t_{\text{acc}})}{\int_0^{t_{\text{acc}}} S(t') dt_1} dt_{\text{acc}} \quad (\text{B18})$$

The corresponding wind heating parameter v_w' and mass return parameter, η' , will be given by

$$\eta' = \frac{\dot{M}'(t)}{\int_0^t S(t_1) dt_1 + \int_0^t A(t_1) dt_1} t_h \quad (\text{B19})$$

$$v_w'^2 = 2 \frac{\dot{E}'(t)}{\dot{M}'(t)} \quad (\text{B20})$$

Figure B2 shows how the wind heating varies as star formation histories deviate from their halo-averaged values. In particular, we show

$$\dot{M}(t) = \int_0^t S(t_1) \dot{m}(t - t_1) dt_1 \quad (\text{B21})$$

$$\dot{E}(t) = \int_0^t S(t_1) \dot{e}(t - t_1) dt_1, \quad (\text{B22})$$

$$\mathcal{V}_w^2(t) = 2 \dot{E}(t) / \dot{M}(t) \quad (\text{B23})$$

In these equations,

$$S(t) = S(t) \times \left(\frac{2}{\pi} (1 - \iota) \arctan(t / \delta t_*) + \iota \right) \quad (\text{B24})$$

This function convolves the recent ($z \approx 0$) halo-averaged star formation history with local variation to give a more pessimistic estimate for the value of \tilde{v}_w . In particular, replacing $S(t)$ with $S(t)$ reduces the recent star formation rate to a fraction ϵ of its halo-averaged value, and does so for a characteristic time δt_* into the past. As we can see in Fig. B2, this dramatically lowers the effective wind speed when both $\delta t_* \gtrsim 10^7$ yr and $\epsilon \lesssim 0.1$, but otherwise has too modest of an effect to change the thermal stability properties of the flow (although the location of r_s and the value of \dot{M} may change significantly).

REFERENCES

- Balbus S. A., 2001, [ApJ](#), **562**, 909
 Berger E., Zauderer A., Pooley G. G., Soderberg A. M., Sari R., Brunthaler A., Bietenholz M. F., 2012, [ApJ](#), **748**, 36
 Blandford R. D., Begelman M. C., 1999, [MNRAS](#), **303**, L1
 Bloom J. S., et al., 2011, [Science](#), **333**, 203
 Bondi H., 1952, [MNRAS](#), **112**, 195
 Bower G. C., Metzger B. D., Cenko S. B., Silverman J. M., Bloom J. S., 2013, [ApJ](#), **763**, 84
 Brandenburg A., 2003, Computational aspects of astrophysical MHD and turbulence. p. 269
 Brighenti F., Mathews W. G., 2003, [ApJ](#), **587**, 580
 Bromberg O., Nakar E., Piran T., Sari R., 2011, [ApJ](#), **740**, 100
 Burrows D. N., et al., 2011, [Nature](#), **476**, 421
 Carson D. J., Barth A. J., Seth A. C., den Brok M., Cappellari M., Greene J. E., Ho L. C., Neumayer N., 2015, [AJ](#), **149**, 170

- Ciotti L., Ostriker J. P., 2007, *ApJ*, **665**, 1038
- Ciotti L., D’Ercole A., Pellegrini S., Renzini A., 1991, *ApJ*, **376**, 380
- Ciotti L., Ostriker J. P., Proga D., 2010, *ApJ*, **717**, 708
- Cuadra J., Nayakshin S., Springel V., Di Matteo T., 2005, *MNRAS*, **360**, L55
- Cuadra J., Nayakshin S., Springel V., Di Matteo T., 2006, *MNRAS*, **366**, 358
- Cuadra J., Nayakshin S., Martins F., 2008, *MNRAS*, **383**, 458
- Cuadra J., Nayakshin S., Wang Q. D., 2015, *MNRAS*, **450**, 277
- Dalton W. W., Balbus S. A., 1993, *ApJ*, **404**, 625
- De Colle F., Guillochon J., Naiman J., Ramirez-Ruiz E., 2012, *ApJ*, **760**, 103
- Di Matteo T., Springel V., Hernquist L., 2005, *Nature*, **433**, 604
- Donas J., et al., 2007, *ApJS*, **173**, 597
- Draine B. T., 2011, *Physics of the interstellar and intergalactic medium*. Princeton series in astrophysics, Princeton University Press, Princeton, N.J.
- Emsellem E., et al., 2007, *MNRAS*, **379**, 401
- Eracleous M., Hwang J. A., Flohic H. M. L. G., 2010, *ApJS*, **187**, 135
- Fabian A. C., 2012, *ARA&A*, **50**, 455
- Ferrarese L., Ford H., 2005, *Space Sci. Rev.*, **116**, 523
- Gallo E., Treu T., Jacob J., Woo J.-H., Marshall P. J., Antonucci R., 2008, *ApJ*, **680**, 154
- Gallo E., Treu T., Marshall P. J., Woo J.-H., Leipski C., Antonucci R., 2010, *ApJ*, **714**, 25
- Gan Z., Yuan F., Ostriker J. P., Ciotti L., Novak G. S., 2014, *ApJ*, **789**, 150
- Gaspari M., Brighenti F., Temi P., 2012a, *MNRAS*, **424**, 190
- Gaspari M., Ruszkowski M., Sharma P., 2012b, *ApJ*, **746**, 94
- Gaspari M., Ruszkowski M., Oh S. P., 2013, *MNRAS*, **432**, 3401
- Gaspari M., Brighenti F., Temi P., 2015, *A&A*, **579**, A62
- Giannios D., Metzger B. D., 2011, *MNRAS*, **416**, 2102
- Graham A. W., Spitler L. R., 2009, *MNRAS*, **397**, 2148
- Greene J. E., et al., 2010, *ApJ*, **721**, 26
- Harper-Clark E., Murray N., 2009, *ApJ*, **693**, 1696
- Heckman T. M., Best P. N., 2014, *ARA&A*, **52**, 589
- Heckman T. M., Kauffmann G., Brinchmann J., Charlot S., Tremonti C., White S. D. M., 2004, *ApJ*, **613**, 109
- Ho L. C., 1999, *ApJ*, **516**, 672
- Ho L. C., 2008, *ARA&A*, **46**, 475
- Ho L. C., 2009, *ApJ*, **699**, 626
- Holzer T. E., Axford W. I., 1970, *ARA&A*, **8**, 31
- Johnson B. M., Quataert E., 2007, *ApJ*, **660**, 1273
- Kauffmann G., Heckman T. M., 2009, *MNRAS*, **397**, 135
- Kippenhahn R., Weigert A., 1990, *Stellar Structure and Evolution*
- Kormendy J., Ho L. C., 2013a, *ARA&A*, **51**, 511
- Kormendy J., Ho L. C., 2013b, *ARA&A*, **51**, 511
- Kormendy J., Richstone D., 1995, *Annual Review of Astronomy and Astrophysics*, **33**, 581
- Kurosawa R., Proga D., 2009, *ApJ*, **693**, 1929
- Lauer T. R., et al., 2005, *AJ*, **129**, 2138
- Lauer T. R., et al., 2007, *ApJ*, **662**, 808
- Levan A. J., et al., 2011, *Science*, **333**, 199
- Li Y., Bryan G. L., 2014a, *ApJ*, **789**, 54
- Li Y., Bryan G. L., 2014b, *ApJ*, **789**, 153
- Li J., Ostriker J., Sunyaev R., 2013, *ApJ*, **767**, 105
- Lorimer D. R., 2013, in van Leeuwen J., ed., *IAU Symposium Vol. 291, IAU Symposium*. pp 237–242 ([arXiv:1210.2746](https://arxiv.org/abs/1210.2746)), doi:10.1017/S1743921312023769
- MacLeod M., Ramirez-Ruiz E., Grady S., Guillochon J., 2013, *ApJ*, **777**, 133
- Maeder A., Meynet G., 1987, *A&A*, **182**, 243
- Manchester R. N., Hobbs G. B., Teoh A., Hobbs M., 2005, *AJ*, **129**, 1993
- Maoz D., Mannucci F., Brandt T. D., 2012, *MNRAS*, **426**, 3282
- McConnell N. J., Ma C.-P., 2013, *ApJ*, **764**, 184
- McConnell N. J., Ma C.-P., Gebhardt K., Wright S. A., Murphy J. D., Lauer T. R., Graham J. R., Richstone D. O., 2011, *Nature*, **480**, 215
- McCourt M., Sharma P., Quataert E., Parrish I. J., 2012, *MNRAS*, **419**, 3319
- McNamara B. R., Nulsen P. E. J., 2007, *ARA&A*, **45**, 117
- Metzger B. D., Giannios D., Mimica P., 2012, *MNRAS*, **420**, 3528
- Miller B. P., Gallo E., Greene J. E., Kelly B. C., Treu T., Woo J.-H., Baldassare V., 2015, *ApJ*, **799**, 98
- Mimica P., Giannios D., Metzger B. D., Aloy M. A., 2015, *MNRAS*, **450**, 2824
- Moster B. P., Naab T., White S. D. M., 2013, *MNRAS*, **428**, 3121
- Naiman J., Soares-Furtado M., Ramirez-Ruiz E., 2013, preprint, ([arXiv:1310.8301](https://arxiv.org/abs/1310.8301))
- Narayan R., Yi I., 1995, *ApJ*, **452**, 710
- Novak G. S., Ostriker J. P., Ciotti L., 2011, *ApJ*, **737**, 26
- Parrish I. J., Stone J. M., 2007, *ApJ*, **664**, 135
- Pellegrini S., 2010, *ApJ*, **717**, 640
- Perez E., et al., 2013, *ApJ*, **764**, L1
- Quataert E., 2004, *ApJ*, **613**, 322
- Rubin D., Loeb A., 2011, *Advances in Astronomy*, **2011**
- Sazonov S. Y., Ostriker J. P., Sunyaev R. A., 2004, *MNRAS*, **347**, 144
- Schödel R., et al., 2007, *A&A*, **469**, 125
- Sharma P., Quataert E., Hammett G. W., Stone J. M., 2007, *ApJ*, **667**, 714
- Sharma P., McCourt M., Quataert E., Parrish I. J., 2012, *MNRAS*, **420**, 3174
- Sharma P., Roy A., Nath B. B., Shchekinov Y., 2014, *MNRAS*, **443**, 3463
- Shcherbakov R. V., Wong K.-W., Irwin J. A., Reynolds C. S., 2014, *ApJ*, **782**, 103
- Spitzer L., 1962, *Physics of Fully Ionized Gases*
- Stone N. C., Metzger B. D., 2014, preprint, ([arXiv:1410.7772](https://arxiv.org/abs/1410.7772))
- Tanaka T., Menou K., 2006, *ApJ*, **649**, 345
- Tchekhovskoy A., Metzger B. D., Giannios D., Kelley L. Z., 2014, *MNRAS*, **437**, 2744
- Thornton K., Gaudlitz M., Janka H.-T., Steinmetz M., 1998, *ApJ*, **500**, 95
- Voit G. M., Donahue M., Bryan G. L., McDonald M., 2015, *Nature*, **519**, 203
- Volonteri M., Dotti M., Campbell D., Mateo M., 2011, *ApJ*, **730**, 145
- Voss R., Diehl R., Hartmann D. H., Cerviño M., Vink J. S., Meynet G., Limongi M., Chieffi A., 2009, *A&A*, **504**, 531
- Yuan F., Li M., 2011, *ApJ*, **737**, 23
- Yuan F., Narayan R., 2014, *ARA&A*, **52**, 529
- Yusef-Zadeh F., Bushouse H., Schödel R., Wardle M., Cotton W., Roberts D. A., Noguera-Lara F., Gallego-Cano E., 2015, preprint, ([arXiv:1506.07182](https://arxiv.org/abs/1506.07182))
- Zauderer B. A., et al., 2011, *Nature*, **476**, 425
- Zhang W. M., Soria R., Zhang S. N., Swartz D. A., Liu J. F., 2009, *ApJ*, **699**, 281
- Zubovas K., Nayakshin S., 2014, *MNRAS*, **440**, 2625
- van Velzen S., Frail D. A., Körding E., Falcke H., 2013, *A&A*, **552**, A5